

Improving Nocturnal Fire Detection With the VIIRS Day–Night Band

Thomas N. Polivka, Jun Wang, Luke T. Ellison, Edward J. Hyer, and Charles M. Ichoku

Abstract—Building on existing techniques for satellite remote sensing of fires, this paper takes advantage of the day–night band (DNB) aboard the Visible Infrared Imaging Radiometer Suite (VIIRS) to develop the Firelight Detection Algorithm (FILDA), which characterizes fire pixels based on both visible-light and infrared (IR) signatures at night. By adjusting fire pixel selection criteria to include visible-light signatures, FILDA allows for significantly improved detection of pixels with smaller and/or cooler subpixel hotspots than the operational Interface Data Processing System (IDPS) algorithm. VIIRS scenes with near-coincident Advanced Spaceborne Thermal Emission and Reflection (ASTER) overpasses are examined after applying the operational VIIRS fire product algorithm and including a modified “candidate fire pixel selection” approach from FILDA that lowers the $4\text{-}\mu\text{m}$ brightness temperature (BT) threshold but includes a minimum DNB radiance. FILDA is shown to be effective in detecting gas flares and characterizing fire lines during large forest fires (such as the Rim Fire in California and High Park fire in Colorado). Compared with the operational VIIRS fire algorithm for the study period, FILDA shows a large increase (up to 90%) in the number of detected fire pixels that can be verified with the finer resolution ASTER data (90 m). Part (30%) of this increase is likely due to a combined use of DNB and lower $4\text{-}\mu\text{m}$ BT thresholds for fire detection in FILDA. Although further studies are needed, quantitative use of the DNB to improve fire detection could lead to reduced response times to wildfires and better estimate of fire characteristics (smoldering and flaming) at night.

Index Terms—Day–night band (DNB), fire detection, fires, gas flares, Visible Infrared Imaging Radiometer Suite (VIIRS), visible light at night, wildfires.

I. INTRODUCTION

AS AN important component in the Earth–atmosphere system, wildfires are a serious threat to life and property that, despite improving warning systems [1], [2], have

Manuscript received September 11, 2015; revised March 2, 2016 and April 25, 2016; accepted May 5, 2016. Date of publication June 23, 2016; date of current version August 2, 2016. This work was supported in part by the NASA Suomi NPP Program and Applied Science Program managed by John A. Haynes and Lawrence A. Friedl and in part by the Interdisciplinary Studies (IDS) Program directed by J. Kaye and administered through the Radiation Sciences Program managed by Hal B. Maring. The work of T. Polivka was also supported by the NASA Nebraska Space Grant.

T. N. Polivka and J. Wang are with the Department of Earth and Atmospheric Sciences, University of Nebraska—Lincoln, Lincoln, NE 68588 USA (e-mail: thomas.polivka@huskers.unl.edu; jwangjun@gmail.com).

L. T. Ellison is with Science Systems and Applications, Inc., Lanham, MD 20706 USA, and also with NASA Goddard Space Flight Center, Greenbelt, MD 20771 USA (e-mail: luke.ellison@nasa.gov).

E. J. Hyer is with the Marine Meteorology Division, Naval Research Laboratory, Monterey, CA 93943 USA (e-mail: edward.hyer@nrlmry.navy.mil).

C. M. Ichoku is with the NASA Goddard Space Flight Center, Greenbelt, MD 20771 USA (e-mail: charles.ichoku@nasa.gov).

Color versions of one or more of the figures in this paper are available online at <http://ieeexplore.ieee.org>.

Digital Object Identifier 10.1109/TGRS.2016.2566665

exacted greater costs in recent years [3], [4]. In addition, they impact global atmospheric chemistry by releasing potent trace gases such as carbon monoxide, carbon dioxide, methane, and ethene [5], as well as aerosols and black carbon [6]. These by-products of combustion are capable of traveling great distances and impacting health and meteorological processes in remote locations [7], [8], and in addition to creating local pollution hazards, these can affect Earth’s climate [9]. Fire-spawned smoke aerosols have complex interactions with the atmosphere by causing a reduction in surface illumination [10]–[12] and simultaneously warming the atmosphere, thereby decreasing vertical temperature gradients and increasing atmospheric stability [13] due to their relatively low single-scattering albedo [14]. As a consequence of wildfire lethality and potential for property damage, earlier detection of wildfires via remote sensing is paramount to proper allocation of fire management resources [15], [16]. Effective response to all of these phenomena requires accurately detecting and characterizing fires as well as accurately quantifying emissions from biomass burning.

The launch of the Suomi National Polar-orbiting Partnership (S-NPP) satellite on 28 October 2011 has opened up unprecedented capabilities with the Visible Infrared Imaging Radiometer Suite (VIIRS) instrument. With a heritage extending back over 40 years to the Defense Meteorological Satellite Program (DMSP) Sensor Aerospace Vehicle Electronics Package (SAP), first launched in 1970, Advanced Very High Resolution Radiometer (AVHRR, first launched 1978), and Moderate Resolution Imaging Spectroradiometer (MODIS, first launched in 1999), VIIRS boasts improved spatial resolution and a higher signal-to-noise ratio than these legacy sensors. VIIRS has already shown promise in detecting smaller and cooler fires [17] than what MODIS currently is capable of. This paper presents a novel approach to detecting fire pixels (with smaller and/or cooler subpixel hotspots) by employing the VIIRS day–night band (DNB) in conjunction with the midwave infrared (MWIR) band that is currently used in both the MODIS and VIIRS fire detection algorithms.

This paper is divided as follows. In Section II, we present a brief history of satellite remote sensing of fires, primarily based on the past research that used AVHRR, Geostationary Operational Environmental Satellite (GOES), and MODIS data. In Section III, the characteristics of VIIRS and its data are described in detail. The ASTER sensor, used for validation, is also described in Section III. Afterward, we discuss the methods employed to improve the detection of smaller and cooler fires in Section IV. We then discuss the results and validation in Section V, and in Section VI, we finish with a discussion of our findings and main conclusions.

II. PRE-VIIRS NASA/NOAA SATELLITE-BASED FIRE DETECTION

Weather satellites have played a pivotal part in the understanding of the Earth–atmosphere system since 1 April 1960, when NASA launched the first weather satellite, i.e., the Television Infrared Observation Satellite (TIROS-1), into orbit. TIROS-1 carried a television camera that only pointed at the Earth for short portions of its orbit (over North America). Convinced by TIROS-1's success in monitoring meteorological conditions, the U.S. Air Force launched its own military satellite program in 1962, i.e., DMSP. Subsequent satellite launches (organized into “blocks” based on satellite generation) improved upon sensor and bus design. In order to monitor nocturnal cloud cover, the DMSP Blocks 5A, B, and C (1970–1975) were capable of observing low-light environments at night with the SAP [18]. The SAP carried two sensors: one for visible and the other for IR radiation. The visible sensor was capable of observing nocturnal scenes as the spectral response was quite broad: the half-power response points were at 0.57 and 0.97 μm with the peak at around 0.8 μm [19]. Data from the nocturnal scenes had a resolution of approximately 3.7 km near the subsatellite point. Using the SAP's visible channel, Croft [20] was the first person to qualitatively demonstrate its potential for monitoring gas flaring, savannah brush fires, and cooking fires over Africa during the night. In 1976, DMSP Block 5D was launched, and carried a new instrument that improved upon the SAP's design: the Operational Linescan System (OLS). Like the SAP, the OLS has a very broad band covering the visible and NIR portion of the spectrum with a “smoothed” spatial resolution of approximately 2.7 km. The instrument was also noted by Croft [21] to be excellent at qualitatively observing gas flares and city lights [22]. The DMSP data were eventually declassified and made available to scientists, who used the sensor to globally map cities, human settlements, and nighttime fires based on their light emission [18], [23], [24].

Unrelated to the DMSP, subsequent NASA TIROS satellites improved upon the original satellite design, and following the collaboration with NOAA, the TIROS-N satellite was launched in 1978. TIROS-N brought digital data transmission, rather than analog as in previous NASA satellites [25]. In addition, TIROS-N carried a powerful instrument for its time: the AVHRR. AVHRR/1 was a scanning radiometer which sensed the Earth in four channels (increased to five on later AVHRR sensors). The four channels spanned several different sectors of the electromagnetic spectrum with a resolution of 1.09 km at nadir [25]: Channel 1 sensed a portion of the visible spectrum (0.58–0.68 μm); channel 2 recorded the NIR (0.725–1.00 μm); channel 3, being a hybrid channel (since NOAA-15), utilized two different IR signatures of 1.58–1.64 μm [channel 3a, shortwave IR (SWIR)] and 3.55–3.93 μm (channel 3b, MWIR); and finally, channel 4 covering 10.30–11.30 μm . Channel 5 (11.50–12.50 μm) was added with AVHRR/2. The AVHRR datastream has continued uninterrupted since the launch of the first one in 1978, giving a remarkable history of how the Earth's surface and atmosphere has changed through the decades.

Using AVHRR's channels 3b (centered at 3.74 μm) and 4 (centered at 10.8 μm), Dozier [26] developed a bispectral approach to identify hot sources and quantitatively estimate the area occupied by the hot target in an unsaturated pixel.

Channel 3b, spanning 3.55–3.93 μm , was noted to be sensitive to hot sources such as steel mills in the Ohio River Valley and gas flares in the Middle East [27]. Flaming wildfires typically have kinetic temperatures between 800 and 1200 K (sometimes as hot as 1800 K) and smoldering temperatures between 450 and 800 K [28]. At a temperature of 1000 K, fire emits radiation with peak radiance at 2.9 μm (according to the Planck function). As smoldering fire ($T = 600$ K) has peak radiation emission at 4.8 μm , the combination of the two combustion types lies very close to the spectrum of AVHRR's channel 3b (3.6–3.9 μm). However, by the same logic, the influence of the fires in channel 4 (10.3–11.3 μm) is small by comparison, which is why it is used to separate fires from background scene brightness effects. In addition to the signal difference between the two channels, the approach also depended on an accurate estimation of a background temperature, e.g., the surface kinetic temperature of the portion of the pixel that was not occupied by the heat source. This was assumed to be represented by the ~ 4 μm brightness temperature (BT) of a similar adjacent pixel [27]. It should be noted, however, that Giglio and Kendall [29] later showed that averaging neighboring pixel BTs for 4 and 11 μm could be used instead of estimating the surface background kinetic temperature. Using the approach in [26], Matson and Dozier [27] performed the first estimation of gas flare and steel mill temperatures and areas using AVHRR's IR bands, as AVHRR was not capable of detecting visible light at night. This was the first time fires were observed from satellite via the IR bands alone. Several studies (including [30] and [31]) used this relationship to investigate the global distribution and frequency of wildfires. Today, fire detection algorithms have evolved from AVHRR into the realm of more sophisticated sensors, but they are still based on that principle: the difference in radiance/BT between 4 and 11 μm [17], [32]–[37].

Several early fire detection algorithms developed for AVHRR identified potential fire pixels according to predefined thresholds (e.g., in [38]–[40]). These consisted of the minimum 3.8- μm BT (abbreviated as BT_4) and a minimum difference between 3.8- μm and 10.8- μm BTs (abbreviated $BT_4 - BT_{11}$) that a pixel must exceed. For example, in [38], any pixel with a BT_4 greater than 311 K and $BT_4 - BT_{11}$ greater than 8 K was flagged as a potential fire. Only then would additional contextual tests be run, which compared the potential fire pixel to its surrounding pixels. These thresholds were usually tailored to the specific region to be monitored (such as subtropical Africa, as in [39]) and had difficulty monitoring fires in radically different environments [41]. Other algorithms, such as those of [38], [40], and [42], employed contextual tests as well to attempt to further screen out false positives while permitting the use of a lower BT_4 threshold. Common to all these algorithms is that they used BT_4 and $BT_4 - BT_{11}$ thresholds that were obtained empirically and somewhat arbitrarily.

Despite AVHRR's power and utility for remotely sensing wildfires globally, it was still largely limited by the large pixel sizes and the fact that fires only occupy a small portion of a full pixel (termed fire fraction). The BT for a pixel consists of the total radiance over the entire pixel area detected by the sensor, which in AVHRR's case, is 1.09 km \times 1.09 km near the subsatellite point [25]. This means most fire signals, although having their peak emission wavelength close to 3.7 μm , are largely drowned out by the background (nonburning) portion

of a pixel. AVHRR's 3b and 4 channels also suffer from low saturation temperatures, which depending on the platform and calibration coefficients, varies between 322 and 331 K [31]. In cases of extremely hot fires/targets, the bispectral approach from [26] readily breaks down [43]. In addition, AVHRR only affords two views per day across much of the globe, because the 3.7- μm channel has not been always available due to the channel 3a3b scheme. Newer instruments would partially overcome these limitations.

Geostationary sensors were in a prime position to supplement the poor temporal resolution of AVHRR, despite their decreased spatial resolution. Beginning in 1980 with the launch of GOES-4, NOAA's GOES systems were equipped with an atmospheric sounder: the Visible and Infrared Spin Scan Radiometer Atmospheric Sounder (VAS). The sensor provided bands centered near 4 and 11 μm , allowing for the use of the Dozier approach (see [26]), despite a significant caveat: The spatial resolution of the VAS was ~ 14 km for the 4- μm band and ~ 7 km for the 11- μm band [33], versus AVHRR's ~ 1 km. However, the large pixel sizes also meant that the sensor did not saturate nearly as frequently as AVHRR. Prins and Metzel [33] developed an algorithm that utilized the VAS to identify biomass burning in South America. Unlike the algorithms that used predetermined BTs as in AVHRR, fire pixels were identified only when BT_4 was 4 K greater than the background BT_4 (termed BT_{4b}) and the BT_{11} was 1 K greater than the background BT_{11} (termed BT_{11b}). They proved that the VAS had immense potential in monitoring biomass fires in South America, and although showing promising results, the technique was too cumbersome to perform on an operational level [33]. At the time, the approach required manual smoke and atmospheric correction to account for differences in atmospheric transmittance caused by the water vapor contained in the smoke. Later, Prins and Metzel [44] released the automated biomass-burning algorithm (ABBA), an updated version of the algorithm developed in 1992 but done on a much larger and automated scale. As before, fire pixels were identified after being compared against the background BTs. Background BTs were 11- μm nonfire BTs calculated from $150 \text{ km} \times 150 \text{ km}$ subsections of the study area after correcting for transmissivity and emissivity. To be classified as fire pixels in the updated algorithm, pixels needed to pass two primary tests: 1) $BT_4 - BT_{11}$ needed to be greater than $BT_{4b} - BT_{11b}$; and 2) $BT_4 - BT_{4b}$ needed to be greater than 2 K or 1.5 times the BT_{4b} standard deviation. This process disqualified 90% of the nonfire pixels [44], and afterward, additional tests were run that accounted for atmospheric transmittance as the VAS bands showed a moderate degree of water vapor contamination. ABBA was later renamed as Wildfire-ABBA (or WF-ABBA), and has been continually updated (to improve the characterization of background surface temperatures by expanding windows for background areas and through iterative use of statistics of local surrounding surface temperatures). It is widely used to monitor wildfires and estimate smoke emissions [7], [45], in addition to extending well beyond its GOES heritage to European and Japanese geostationary sensors.

One of the most important fire-detecting spaceborne sensors to date, i.e., MODIS, was launched in 1999 aboard NASA's Terra satellite. MODIS is a 36-channel instrument, which covers a wide segment of spectrum from 0.4 to 14.4 μm , with spatial resolutions of 250 m (bands 1–2), 500 m (bands 3–7),

and 1 km (bands 8–36). A second MODIS instrument was launched in 2002 aboard the Aqua satellite. Together, Terra and Aqua provide two to four daylight scenes over much of the globe each day (and two to four more at night). While MODIS was designed for a wide variety of scientific applications, its 3.9 and 11- μm channels were specifically designed for fire detection with saturation temperatures of 450 and 400 K, respectively [46]. The MODIS fire detection algorithm, like the AVHRR algorithms before it, is based on the idea that the BT_4 band is more sensitive to fires than the BT_{11} band [34]. It has undergone numerous revisions over the years, and the latest publicly available version at the time of this study in 2015—MODIS Collection 5—still relies on prespecified thresholds. The original MODIS fire detection algorithm consisted of a combination of absolute and relative tests [34], [47] and was designed to minimize false positives. Giglio *et al.* updated the MODIS algorithm and greatly enhanced its performance with detection of smaller and cooler fires [35]. The primary mechanisms of improvement were lowering the thermal thresholds and including contextual tests, which compared potential fire pixels to their surroundings.

MODIS ushered in an unparalleled level of satellite-based fire research, not only in terms of fire detection but also fire characterization as well. Kaufman developed the concept of fire radiative power (FRP) [46], [47]. FRP, which is a proxy measure of fire intensity based solely on a ~ 4 - μm channel [37], [46], [48], was shown to be correlated with smoke emissions [6], [49]. The MODIS fire products were a substantial upgrade when compared with products from AVHRR and other sensors. By identifying the utility of satellite-based fire detection for fire suppression resource allocation, the U.S. Forest Service requested quicker availability of the MODIS fire products. The MODIS Rapid Response fire product was created as a result, which disseminated fire data within hours of MODIS data acquisition [34]. Until that point, satellite data were useful for fire monitoring but not for detection and response.

While fires were first seen and thought to be detectable by satellite with visible data observed at night [20], quantitative characterization and detection of fire activity from space over the last 40 years has mainly relied on satellite-measured IR data. Here, we take advantage of the DNB's high spatial resolution of ~ 750 m and radiometric calibration aboard VIIRS and continue working toward the ideas that Croft [20] proposed over 40 years ago: combining both visible and IR data to detect fires, creating the FILDA. The remaining sections of this paper describe the data sources, data processing algorithm, and validation results for the FILDA method.

III. INSTRUMENTS AND DATA

A. VIIRS

VIIRS was launched on 28 October 2011, and is a successor to MODIS (used by NASA for quasi-operational fire detection) for operational fire detection. Located aboard S-NPP, VIIRS is a 22-band scanning radiometer with a nominal spatial resolution of 375 m in the five imagery bands (I-bands) and 750 m in both the 16 moderate resolution bands (M-bands) and the DNB [17], [36], [50], [51]. The sensor data records (SDRs) of calibrated radiances and BTs cover a spectral range from

0.411 to 11.87 μm and are used in a wide range of Earth observation applications including fire detection and characterization, retrieval of cloud and aerosol properties, and land and sea surface temperature estimation [52]. The VIIRS sensor was designed to improve upon legacy instruments, such as MODIS, AVHRR, and the OLS. One significant enhancement relative to these legacy sensors is that VIIRS pixels at the scan edge are only four times the size of nadir pixels, compared with MODIS which exhibits a growth factor of nearly ten. For the M-bands, VIIRS delivers SDRs of calibrated radiances and BTs with an instantaneous field of view (IFOV) of 0.74×0.78 km at nadir, which increases to 1.60×1.58 km at the edge of the scan [50], whereas the five imagery bands have smaller IFOVs ranging from 0.37×0.39 km at nadir to 0.80×0.79 km at the scan edge.

Like the OLS, in order to reduce off-nadir pixel growth, VIIRS aggregates samples depending on the sensor scan angle. This is accomplished by employing asymmetrical detectors in conjunction with a unique sample aggregation scheme, which combines multiple samples from one rectangular detector into single raw data record (RDR) pixels consisting of digital counts (see [53, Fig. 1] for an illustration). This processing is done onboard the satellite, except for the dual-gain bands (M1-5, 7, and 13) whose aggregation is done on the ground [51]. As a result, the RDR has three aggregation zones. The 3:1 aggregation zone refers to scan angles between 0° (nadir) and 31.72° , where the value of each pixel is actually the average of three individual samples. Similarly, in the 2:1 aggregation zone (scanning angles between 31.72° and 44.86°), two samples from the same detector are aggregated to form a pixel. No sample aggregation is performed in the 1:1 aggregation zone (scan angles greater than 44.86°); thus, each pixel is calculated from a single detector sample. Once the RDR has been generated, it is later processed into a calibrated SDR, retaining the characteristics from aggregation [53].

Unlike MODIS, VIIRS is able to detect visible light and NIR radiation at night with the DNB. The band has a broad spectral response ($0.5\text{--}0.9$ μm) that is sensitive to city lights, volcanoes, lunar illumination, and wildfires, in addition to phenomena such as aurora, bioluminescence, and air glow, for example [54]–[57]. In order to capture the wide range of radiances reflected and emitted from the Earth's surface, the DNB employs three modes of operation: low-gain, medium-gain, and high-gain stages (the latter of which contains two redundant focal plane arrays to eliminate noise). The low-gain stage is used for sunlit areas, the medium-gain stage is used for twilight areas, whereas the high-gain stage is used for nocturnal scenes. These gains are automatically determined by the onboard electronics module, which can switch between the four focal plane arrays on the fly. In addition to its wide dynamic range, the DNB also features a nearly constant IFOV across the swath, accomplished by employing 32 different aggregation zones for its 672 time-delay-interval detectors [57]. At nadir, the 672 detectors scan the Earth, and 42 detectors are aggregated to comprise each of the 16 pixels per scan. At the edge of the scan, due to the growth of the detector footprint, only the central 320 detectors are aggregated to form the 16 pixels (20 detectors per pixel). Thus, the DNB pixels are coterminous with the M-bands only at nadir; away from nadir, the DNB and M-band pixel boundaries are offset, as explained by their independent aggregation modes.

B. ASTER

In order to evaluate our proposed algorithm, a different sensor with a higher spatial resolution to observe smaller fires must be used. Many past fire studies have opted to use airborne sensors such as the Airborne Infrared Disaster Assessment System in [58] or the Autonomous Modular Sensor in [37], for several reasons. These include their extremely high spatial resolutions, the reduced severity of atmospheric contamination, and ability to plan near-coincident overpasses. There is no supplemental airborne data set to compare with VIIRS data, unfortunately; thus, a different spaceborne sensor is needed to be utilized. The Advanced Spaceborne Thermal Emission and Reflection (ASTER) instrument aboard NASA's Terra satellite proved to be a viable option. ASTER is capable of supplying 90-m thermal IR data at night in five bands across a 60-km swath with a descending equator local crossing time of 10:30 A.M.. Using 12-bit quantization, it supports a 4.2-mb/s data rate to relay the information sensed by its ten Mercury–Cadmium–Tellurium detectors. The longwave bands must be used as the SWIR and visible data collection is turned off for nocturnal scenes. Unfortunately, longwave emissive bands are much less sensitive to fires than shorter wavelengths as described by the Planck function. In [59], it was shown that ASTER's shortest TIR band, band 10 (spanning $8.125\text{--}8.475$ μm , 90 m resolution), was still able to detect fires in the daytime, but was less able to detect individual fires and show less detail than SWIR band 9 ($2.36\text{--}2.43$ μm , 30-m resolution) because of the coarser resolution. Thus, given the nocturnal nature of this paper, band 10 was used. This channel is sensitive to water vapor, but there is still a substantial fire signal nonetheless when compared with the background radiation (as shown in [60]). ASTER data are distributed freely by the USGS.

Nighttime ASTER data are sparse and originate from a different orbit than VIIRS; therefore, overpasses capturing an active fire event also captured by VIIRS are rare. The USGS's Global Visualization Viewer website assisted in visualizing the ASTER data and manually identifying scenes containing fires. While the VIIRS swath overlap does not extend into the ASTER track at the equator, it is indeed possible at higher latitudes that one VIIRS swath may have some overlaps with two or more ASTER tracks. For this paper that focuses on the midlatitude fires, only ASTER scenes that are spatially nearest to the VIIRS nadir view (with temporal differences of less than 4 h) are used to evaluate the VIIRS fire detection. Note that the geolocation tie points packaged with the ASTER granules were consistently mismatching the true geolocation by up to two tenths of a degree; therefore, the data were manually projected using the "SceneFourCorners" metadata, by a process outlined in the ASTER data handbook (http://asterweb.jpl.nasa.gov/content/03_data/04_Documents/aster_user_guide_v2.doc). Once an ASTER scene was found containing a fire, a corresponding VIIRS scene nearest to nadir was obtained.

IV. DATA PROCESSING AND ALGORITHMS

Due to the different aggregation schemes and differing IFOVs between the DNB and M-bands, VIIRS data need to be processed in several ways before they can be used in the fire detection algorithm. In addition, further processing is needed to

account for pixel overlap, despite the onboard overlap deletion (bow-tie deletion). We first describe these procedures and then discuss the VIIRS fire algorithm and our modifications to it by adding the DNB.

A. VIIRS Data Processing

1) *Exclusion of Redundant Overlapping Pixels:* Because of the instrument's wide scanning range, regions far from nadir are often scanned twice, creating a "bow-tie" effect. To reduce downstream bandwidth requirements, the VIIRS flight software automatically excludes some of these duplicate pixels from transmission as a function of aggregation zone. This bow-tie deletion removes the topmost and bottommost pixels from each scan in the 2:1 aggregation zone ($31.72^\circ < \text{scan angle} < 44.86^\circ$), and in the 1:1 aggregation zone (scan angle $> 44.86^\circ$), the top two and bottom two pixels are removed. For perspective, 13% of a given VIIRS granule has data removed by bow-tie deletion. However, despite this bow-tie deletion, significant pixel overlap still occurs near the edge of the scan and before the switch between each aggregation regime (see [51, Fig. 3] for an illustration).

Correcting for this scan overlap is the first obstacle, and the aggregation scheme for the M-bands makes this increasingly complicated. While viewing fires from different geometries can be advantageous [61], it artificially inflates fire retrievals. Therefore, to avoid spuriously double-counting fire pixel detections, overlapping pixels are removed by exploiting the geometric similarities in VIIRS scans. The method is similar to that in [37], except that it is applied to VIIRS instead. One M-band VIIRS scan consists of 3200 along-scan pixels and 16 along-track pixels; however, to accommodate aggregation, each scan is actually comprised of 6304 along-scan samples by 16 along-track samples. In order to make the overlap calculation feasible, the sample dimensions are first determined using VIIRS geometry and by making several assumptions, including that the Earth is a perfect sphere, the orbit is perfectly circular, and excluding terrain influences. Samples in one scan that overlap the subsequent scan boundaries by more than 50% of the samples' along-track dimension are then excluded from the scene. Afterward, the nonoverlapping samples are aggregated into pixels according to VIIRS specifications. This resultant exclusion mask is then applied to the data for each VIIRS scan. After overlap correction, for one scan, only seven rows of along-scan pixels suffer from no overlap by the edge of the scan; the remaining nine rows experience some degree of overlap. Since each scan follows the same scanning geometry, it can be quickly applied to the entire data segment (granule); although close to the poles, there is additional uncertainty. With the 13% onboard bow-tie deletion, after manually correcting for pixel overlap, an additional 11% is removed; thus, a total of 25% of the granule's pixels are removed due to overlap. Unlike the VIIRS operational algorithm that FILDA is based on, if a pixel falls within the 11% of pixels additionally removed, it is not considered for fire pixel detection.

Fig. 1, picturing the Souris River in North Dakota with a scan zenith angle of $\sim 50^\circ$, shows the same sequence of scans before and after correcting for pixel overlap. The black lines in Fig. 1(a) are the bow-tie deleted areas, which is done onboard the satellite according to VIIRS data processing procedures

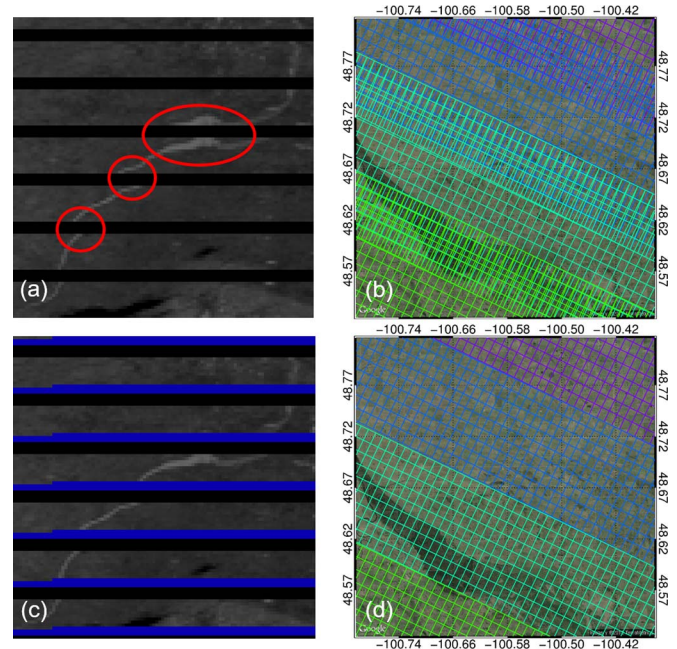


Fig. 1. Correcting for pixel overlap. (a) VIIRS unprojected M13 (BT_4) scene before corrections. The red outlines highlight the duplicated river areas, and black lines are the bow-tie deleted areas done onboard VIIRS. (b) Pixel footprints for the M13 VIIRS scene including overlap (before corrections) with different colors representing different scans. (c) Image in (a) after corrections with additional overlapping regions removed (blue). (d) Projected scans after corrections. Without overlap correction, the same pixel is often counted twice near the edge of the scan.

[62]. As seen by the repeating river pixels circled in red, it is clearly imaging the same area twice, despite the bow-tie deletion (black lines). Fig. 1(b) shows the individual pixel footprints when the same region is enlarged, highlighting the need for overlap correction. Fig. 1(c) and (d) shows the resulting scene after correction, with minimal resulting gaps or overlap.

2) *Resampling DNB Radiances to M-Band Resolution:* After correcting for pixel overlap, normalizing the DNB to M-band pixel sizes is necessary due to their different aggregation schemes and IFOVs. Similar to overlap correction, this approach employs the similarity of VIIRS scans to quickly match the DNB to the M-bands. First, one scan of 16 along-track pixels is analyzed. Since VIIRS is polar-orbiting with an inclination of 98.7° , as the satellite descends in its nighttime orbit, the primary along-scan axis of change is the longitude (excluding extremely high latitudes, which fortunately do not have many fires). Pixel longitudes are taken from the M-band terrain-uncorrected geolocation since there is no DNB terrain-corrected geolocation available for the study period. For each M-band pixel, the left and right edge longitudes are determined by taking the midpoint between neighboring pixels, and then the DNB pixels that fall within that M-band pixel's edges are averaged based on the respective DNB pixel longitude edges. DNB pixels that lie between two M-band pixels have their respective fractions combined into the appropriate M-band pixel. However, since there is still considerable M-band footprint growth in the along-track direction far from nadir (and not in the DNB), they must also be combined in the along-track direction as well using the same principles. After this has been done for one full scan, the calculated geometry and fractions are

then used to correct the remaining scans in the granule. Terrain-corrected geolocation can then be utilized for the M-band and resampled DNB radiances from this point forward. Our method is different than other approaches; for example, in [63], they collocate the DNB pixel with M-band pixels based upon the scan angle and local features (such as data maxima) in each scan line. This dismisses the reality that the DNB maintains a near constant IFOV with almost no pixel overlap, whereas the M-bands overlap significantly, creating a large discrepancy in retrieved geolocation.

B. VIIRS Fire Detection Algorithm

Currently, the VIIRS Interface Data Processing System (IDPS) fire detection algorithm (called the Active Fire Application Related Product or AFARP) is based almost exclusively on the MODIS fire detection algorithm presented in [35], which is the equivalent of the MODIS Collection 4 [36], [64]. As mentioned in Section II, the algorithm is tuned to be conservative and reduce false positives. AFARP was the only VIIRS fire product available during this study period; however, newer products include those generated from NOAA's S-NPP Data Exploitation (NDE) system that started in early 2016, as well as the VIIRS fire products generated within NASA's production systems.

As shown in Fig. 2, the nighttime version of the algorithm begins by using an internal cloud mask to filter out pixels with a BT_{12} (M16) less than 265 K. In addition, any pixels that are known to be water (based on a static database) are filtered out, and any pixels with missing or invalid data are removed. Afterward, the algorithm selects pixels that could be fires, which is any unfiltered pixel with a $BT_4 > 305$ K and $BT_4 - BT_{11} > 10$ K. If any pixels meet those criteria, they have their background statistics calculated, analyzing the pixel's environment relative to neighboring pixels. The background statistics include the calculation of the mean, median, standard deviation, and the mean absolute deviation—used due to its insensitivity to outliers [65]—by a kernel centered on the pixel. The kernel is initially calculated with 3×3 pixels and expands up to a maximum of 21×21 pixels, until at least 25% of the included pixels are valid with a minimum of 8 pixels in total [35]. In this case, valid pixels have a $BT_4 < 310$ K, a $BT_4 - BT_{11} < 10$ K (e.g., not a potential fire pixel), are not cloudy, and are land. If the grid's size reaches 21×21 pixels without satisfying these criteria, the individual pixel it is centered on is flagged as *unknown*. Once the statistics are generated for each potential fire pixel, then four tests are applied to the pixel to determine if it is a fire. The first test is the “absolute” test, and the pixel is flagged as a fire if $BT_4 > 320$ K. If the pixel does not pass the test, then the other three contextual tests are applied, and a pixel must pass all three to be flagged as a fire. They are:

- 1) $\Delta BT > \Delta BT_B + 3.5\delta(\Delta BT_B)$;
- 2) $\Delta BT > \Delta BT_B + 6$ K;
- 3) $BT_4 > BT_{4B} + 3\delta BT_{4B}$;

where ΔBT is $BT_4 - BT_{11}$, ΔBT_B is the background $BT_4 - BT_{11}$, $\delta(\Delta BT_B)$ is the background mean absolute deviation of $BT_4 - BT_{11}$, BT_{4B} is the mean background BT_4 , and δBT_{4B} is the background mean absolute deviation for

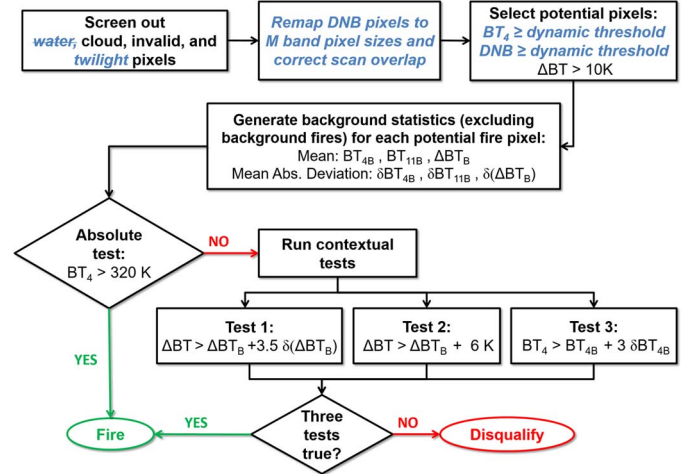


Fig. 2. Flowchart of FILDA, which is based on the operational nocturnal VIIRS fire product (AFARP). Blue text highlights modifications to the algorithm in contrast to AFARP.

BT_4 . During the daytime, there are additional tests to disqualify pixels due to sun glint, unmasked water pixels, and deserts, but they require solar reflectivity and are not utilized at night [35]. After the fire pixels have been identified, they are cataloged. AFARP contains the columns and rows, latitudes and longitudes, and the quality flag data for each fire pixel. Nonfire or disqualified potential fire pixels are not included in the product. Although MODIS Collection 4 is now obsolete, VIIRS is able to overcome some of its shortcomings due to its improved spatial resolution. However, despite the improved spatial resolution, it still relies on a prespecified $4\text{-}\mu\text{m}$ BT threshold of 305 K for potential pixel selection, omitting smaller and cooler fires, irrespective of the environment they are located in.

C. FILDA

Our approach is similar to that of Giglio *et al.* [35] and JPSS [64] with three important differences. First, instead of relying on a prespecified BT_4 threshold of 305 K, FILDA generates the BT_4 threshold dynamically using a moving window around each candidate fire pixel. Second, visible light is also included in the potential fire pixel selection process. Finally, we do not screen out water pixels to capture gas flares and other phenomena such as island volcanoes since sun glint is not an issue at night. The basis for this methodology is that pixels with visible light emission and relatively pronounced BT_4 signatures are likely to be fires (or volcanoes in some cases).

Initially, FILDA and AFARP begin nearly the same by screening out invalid pixels such as clouds and bad data, although FILDA does not exclude water pixels. An added step for FILDA is also filtering out pixels with a solar zenith angle less than 100° , fully removing all twilight areas and thus focusing on the fire detection at night only. Afterward, the overlap correction is applied, and the DNB is collocated with the M-bands. Next, unlike in AFARP, dynamic thresholds are determined. They are computed as follows.

- 1) For an entire granule, determine the minimum DNB radiance threshold. Bin the DNB radiances into increments

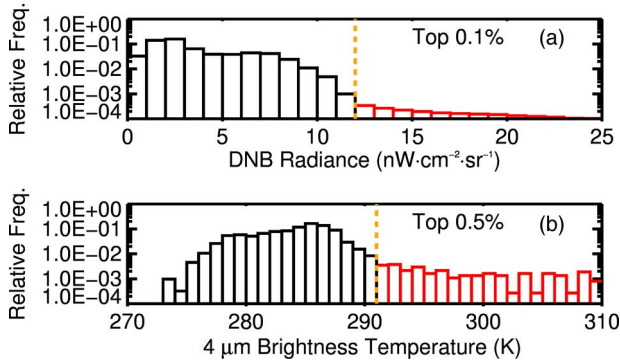


Fig. 3. Histogram of valid DNB radiance values for the nighttime 24 August 2013 granule of the Western United States (orbit 9449, top panel), in addition to the BT_4 distribution for a 61×61 pixelwide box centered on a Rim Fire pixel (bottom panel). The orange dashed line represents the thresholds calculated for this granule. Red rectangles indicate bins that exceed the respective threshold requirement and are included in potential fire pixel selection process.

of $1 \text{ nW} \cdot \text{cm}^{-2} \cdot \text{sr}^{-1}$ and select the lowest bin of the most radiant top 0.1%, with a floor of $4 \text{ nW} \cdot \text{cm}^{-2} \cdot \text{sr}^{-1}$ (usually in a completely moonless scene).

- 2) For an entire granule, filter out pixels with a ΔBT less than 10 K and with DNB radiances less than the respective threshold.
- 3) For the remaining pixels (if any), create a 61×61 pixelwide box around each. Then, bin those BT_4 s in increments of 1 K, and in order of decreasing temperature, select the last bin with a density less than 19 pixels. That bin is then the BT_4 threshold.

After the identification of potential fire pixels, FILDA proceeds exactly as AFARP by running the same absolute and contextual tests. No additional tests are added. At the end, fire pixel latitudes, longitudes, columns, and rows are cataloged. By lowering the BT_4 threshold while still keeping the same ΔBT , FILDA will improve the detection of fire pixels that have cooler BT_4 s (and/or cooler background temperatures [49], [66]). The FILDA algorithm, however, has the same efficiency as AFARP for detecting fire pixels with warmer temperatures; this is because those detected by AFARP (with BT_4 s > 305 K) would pass FILDA's fire detection criteria regardless (where BT_4 is dynamically set and is lower than 305 K). An important caveat, however, is that significant reductions in BT_4 thresholds suffer from diminishing returns. Since the ΔBT threshold must still be greater than 10 K, background temperatures must be exceedingly cold in order to meet that criterion (which intuitively reduces the likelihood of fires).

As an example of how the algorithm operates, a granule containing most of the West Coast of the U.S. on 24 August 2013 (taken during a night of intense burning over the Rim Fire) has a median DNB radiance of $2.4 \text{ nW} \cdot \text{cm}^{-2} \cdot \text{sr}^{-1}$. However, the lowest bin of the top 0.1% most radiant pixels gives a DNB radiance threshold of $12 \text{ nW} \cdot \text{cm}^{-2} \cdot \text{sr}^{-1}$ (see Fig. 3). After screening out pixels less radiant than $12 \text{ nW} \cdot \text{cm}^{-2} \cdot \text{sr}^{-1}$ and with ΔBT s less than 10 K, of the 9.83×10^6 original pixels, 189 pixels remain. Each has its own BT_4 threshold, varying from 284 K for a fire complex in the mountains of Idaho to 293 K in the center of Rim Fire. These 189 potential pixels are then passed to the fire tests, as in AFARP.

This approach has the benefit of selecting a BT_4 threshold that is unique to the environment that each potential fire pixel

is located in. Other thresholds varying from 1% to 0.01% were investigated for both the BT_4 and DNB thresholds, as well. The top 0.5% threshold for BT_4 generally reflected the precipitous decline in frequency for the ~ 50 cases examined. Reducing the BT_4 threshold below 0.5% rapidly increased thresholds, with most BT_4 thresholds in hot regions not much lower than AFARP's static BT_4 threshold of 305 K, and in some cases, exceeding it. Conversely, increasing the BT_4 threshold above 0.5% decreased the resulting thresholds, making them somewhat insensitive to BT_4 distributions, and greatly increasing the potential fire pixel counts. Thus, 0.5% was selected as a conservative threshold. In the given example (see Fig. 3), of the 189 potential fire pixels in the granule which meet all of the prescreening criteria, 180 also passed all contextual tests. While the determined BT_4 thresholds can be quite low (as low as 284 K in some cases examined), they are still necessary to screen out regions adjacent to cloud edges. In most cases, the DNB threshold is primarily influenced by moonlit terrain and low-level clouds not screened by the internal cloud mask due to their higher BT_4 s. Unfortunately, constructing a box around each potential fire pixel means that the scan edges cannot be analyzed as they would exceed the dimensions of the granule.

The end result of the change in potential fire pixel selection criteria is that the potential pixels must have three properties: They are among the 0.5% hottest pixels in their 61×61 pixelwide box, they are also among the 0.1% most radiant DNB pixels of the entire granule, and finally, they must all have a ΔBT of at least 10 K. In the case that a pixel is hotter than 305 K in $4 \mu\text{m}$ without meeting the DNB threshold, it is still marked as potential fire pixel just as in AFARP (assuming $\Delta BT > 10$ K). For example, using the data in Fig. 3, if a pixel has a $BT_4 = 299$ K, a DNB value $= 16 \text{ nW} \cdot \text{cm}^{-2} \cdot \text{sr}^{-1}$, and $\Delta BT = 12$ K, it would be considered a potential fire pixel; however, if the DNB radiance value is $10 \text{ nW} \cdot \text{cm}^{-2} \cdot \text{sr}^{-1}$ instead, it would not be considered as one. Likewise, if a pixel has a $BT_4 = 289$ K and $\Delta BT = 11$ K but has a DNB value of $25 \text{ nW} \cdot \text{cm}^{-2} \cdot \text{sr}^{-1}$, it would also not be considered a potential fire pixel. However, if the BT_4 was 308 K, $\Delta BT = 11$ K, and DNB $= 7 \text{ nW} \cdot \text{cm}^{-2} \cdot \text{sr}^{-1}$, it would be considered a potential fire pixel and analyzed further.

V. RESULTS

Several case studies are presented to show FILDA's potential of using visible light at night to improve fire detection, ranging from large forest fires to gas flares. They are chosen based on three factors: 1) environmental variety representation; 2) availability of near-coincident ASTER overpasses; and 3) the impact level of the fire. Here, we examine California's Rim Fire, which burned in the summer of 2013; the High Park Fire in Colorado from the summer of 2012; and gas flares in the Khanty-Mansiysk and Niger Delta regions from the summer and winter of 2013, respectively.

A. Rim Fire

Located near Yosemite National Park in the Sierra Nevada Mountains in California, the Rim Fire was the third largest wildfire in California's history. It was ignited at 3:25 P.M. (local time) on 17 August 2013 by a hunter's illegal campfire. While it grew slowly at first, the fire grew rapidly on 19 August

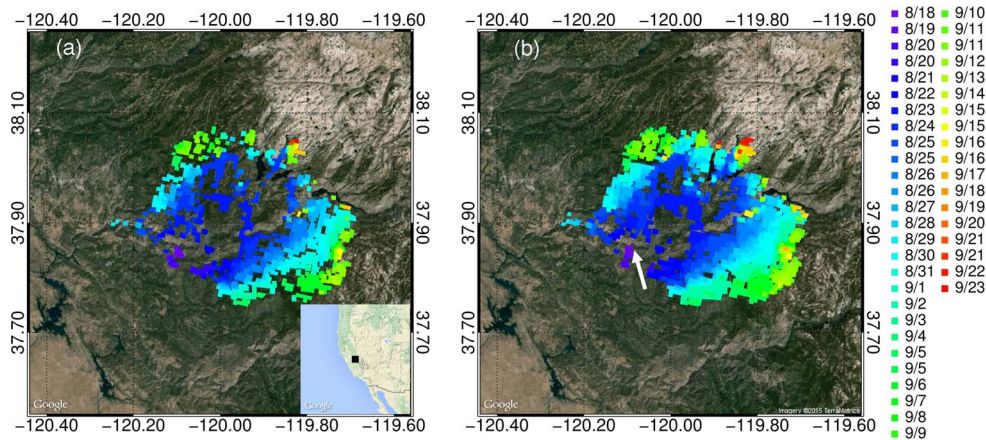


Fig. 4. Progression of the Rim Fire from ignition to extinction. The left panel shows the Rim Fire's development using AFARP, whereas the right panel shows the fire's progress using FILDA. The white arrow highlights the first nocturnal detection by VIIRS using FILDA at 2:43 A.M. PDT on 18 August 2013, 11 h after ignition. AFARP was not able to identify the fire at night until 19 August. Some dates are repeated due to consecutive overpasses on the same days.

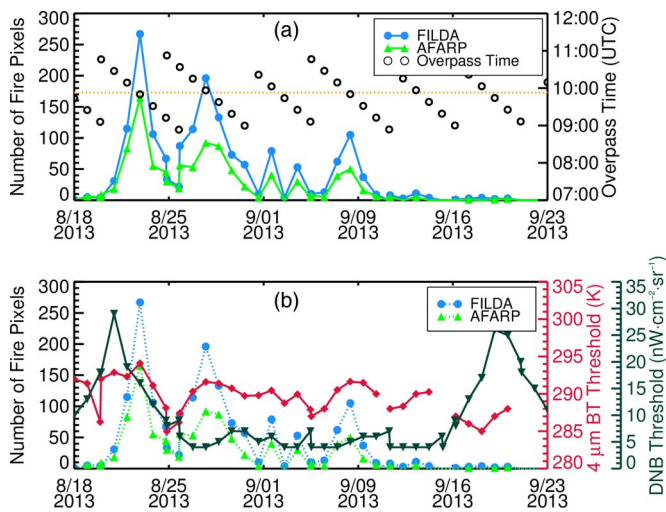


Fig. 5. Time series of fire pixel counts as they relate to overpass time (a) and thresholds (b) over the Rim Fire. FILDA pixel counts are displayed in blue, while AFARP counts are shown in light green. Missing symbols indicate no fire detections for that overpass with the corresponding algorithm. While there is a DNB threshold for every point, there are gaps in BT_4 thresholds due to the lack of potential fire pixels. In addition, the reduced overpass frequency near 1 September 2013 is because the Rim Fire was too close to the granule edges.

and then explosively a week after ignition. The Rim Fire's rapid growth was primarily driven by favorable upper air conditions, which created sustained low relative humidity and strong winds near the surface, particularly during nighttime hours [67]. By the time it was extinguished, it had burned over 250 000 acres of forest within one month.

VIIRS provides a unique vantage point to study the Rim Fire because of its ability to track the smoke and light emissions at night. Because the fire continued to grow quickly during nocturnal hours, the Rim Fire is an ideal candidate for FILDA application. After applying FILDA to every VIIRS scene covering the Rim Fire during its burn duration (51 granules), Fig. 4 shows the comparison between AFARP (left) and FILDA (right) fire pixel detections. The first major difference between the two is that FILDA is able to detect the Rim Fire the first night it burned, with an overpass time of 2:43 A.M. PDT on 18 August 2013. AFARP is unable to identify the fire because the pixel's $4\text{-}\mu\text{m}$

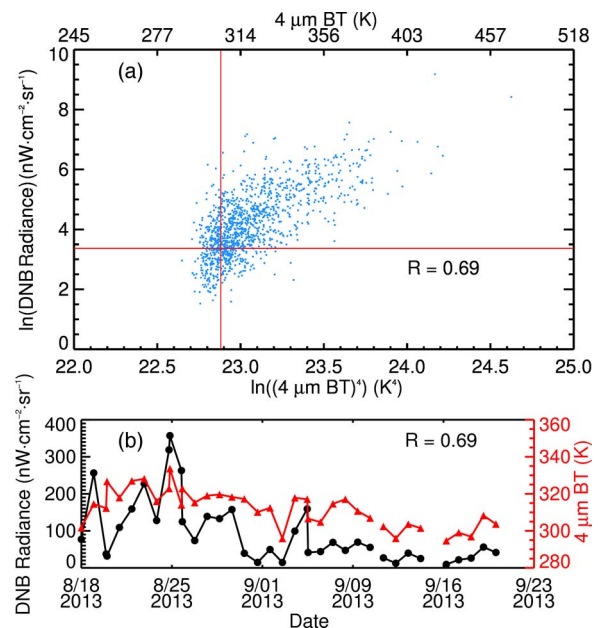


Fig. 6. (a) Scatter plot of BT_4^4 and DNB radiances for FILDA fire pixels from the 3:1 aggregation zone for the Rim Fire during the 8 August–23 September 2013 period. Note the logarithmic scale for both the x-axis and y-axis. Moreover, shown is the linear correlation coefficient (R) between the two variables. The vertical and horizontal lines in red denote the BT_4 threshold (305 K) used in AFARP and the maximum value of the DNB thresholds used by FILDA during the whole Rim Fire time period, respectively. (b) Time series of mean DNB radiance (left y-axis) and BT_4 (right y-axis) for fire pixels detected by VIIRS for each day.

BT is only 301.7 K, which is 3.3 K below the minimum detection threshold. Meanwhile, FILDA's $4\text{-}\mu\text{m}$ BT threshold is 292 K with a DNB threshold of $10\text{ nW}\cdot\text{cm}^{-2}\cdot\text{sr}^{-1}$. Comparing the two maps, a distinct pattern can be seen: The growth of the Rim Fire is better tracked using FILDA. The large gaps in coverage for both images occur due to a period of explosive growth between 3:27:26 A.M. PDT on 21 August 2013 to 3:04:14 A.M. PDT on 22 August 2013, during which the fire tripled in area burned.

As mentioned, FILDA's BT_4 and DNB thresholds are dynamic. Fig. 5 shows how the pixel counts and thresholds vary with each scene and scanning geometry. The top graph relates

TABLE I
PIXEL COUNTS OF DETECTED HOTSPOTS OVER THE COURSE OF THE
RIM FIRE FOR AFARP AND FILDA BY AGGREGATION ZONE

Algorithm	1:1 zone	2:1 zone	3:1 zone	Total
Detected by both ¹ :	91	167	659	917
Only detected by FILDA:	116	130	584	830
Only detected by AFARP:	51	15	27	93

¹ The same pixel sample was classified as a hotspot by both AFARP and FILDA.

the pixel counts for FILDA and AFARP in relation to scan angle; as with any other scanning radiometer, geometry plays a significant role in time series of retrievals (e.g., [68]). Near-nadir cases are closest to the horizontal orange dotted line. These nadir cases show obvious peaks in fire pixel retrievals, for both FILDA and AFARP, since there are more pixels encompassing the fire region. Farther from nadir, fire pixel frequencies are considerably reduced. It should be noted that this effect will be smaller than for MODIS because of the reduced pixel footprint growth rate due to the VIIRS aggregation scheme. The bottom graph shows how the DNB and mean BT_4 thresholds vary with each scene. Overall, the BT_4 threshold varies between ~ 285 and ~ 295 K; note that the very top of the $4\text{-}\mu\text{m}$ axis is the threshold for AFARP. Rapid shifts in overpass time reflect that the Rim Fire has been scanned twice in one night due to being close to the scan edge in two consecutive orbits, although the influence is minor. Unlike the BT_4 threshold, the DNB threshold is primarily governed by the lunar cycle. This is because moonlit terrain effectively raises the signal floor, increasing the minimum DNB radiance for the top 0.1%. For moonless or nearly-moonless scenes, the top 0.1% instead captures the effects of artificial lights.

In addition, the FILDA's performance in comparison to AFARP has been quantified in Table I. Throughout the lifetime of the Rim Fire, both algorithms agreed on most hotspot detections in the VIIRS' 3:1 and 2:1 aggregation zones along the scan direction. Near the center of the scan (3:1 aggregation), FILDA was able to increase the number of hotspot detections by 89%. However, significant divergence occurred in the 1:1 aggregation zone (near the edge of the scan). This is due to two factors. First, larger pixel areas decrease fire fractions and diminish hotspot signals, which FILDA is better able to capture due to the reduced thermal thresholds. Second, this divergence is related to FILDA's scan overlap correction. The number of pixels only detected by AFARP (93 in total, bottom row of Table I) consists entirely of fire pixels that were disqualified by overlap correction.

Fig. 6(a) shows a scatter plot of DNB radiances and BT_4 s for all FILDA Rim Fire pixels from the 3:1 aggregation zone (1243 in total). This figure highlights an important issue with the version of AFARP used during the study period: many of the pixels identified by FILDA hotter than 305 K were excluded by AFARP (301 pixels in total), despite successfully satisfying all required criteria. This has been relayed to the Active Fire team for further analysis. In addition, while overlap correction can partially explain the difference in fire pixel detections, the use of the DNB to dynamically lower the BT_4 threshold from 305 K is a major reason for large increases in fire pixel detections by FILDA (middle row in Table I). Despite overlap

correction, FILDA adds 283 more fire pixels as shown on the left side of the vertical line. In other words, $\sim 30\%$ more fire pixels are detected by FILDA because of the combined use of the DNB and a dynamic BT_4 threshold (if FILDA and AFARP were to agree on all detections greater than 305 K). Furthermore, by adding a horizontal line representing the maximum DNB threshold during Rim Fire with the vertical BT_4 threshold line, we can divide Fig. 6 into four quadrants to better classify fire pixels. Most (65%) of the fire pixels are in the upper right quadrant, indicating they are hot and bright, meaning subpixel hotspots are likely in the flaming phase. Twelve percent of the fire pixels are in the lower right quadrant, indicating they are relatively hot but not very bright. Many factors affect the distribution of BTs and DNB radiances at the pixel level (including fire fraction, kinetic temperature, terrain, emissivity, smoke cover, and so on), but this suggests that the flaming fraction could be lower and the smoldering fraction could be higher than the upper right quadrant. Another 12% of fire pixels are in the upper left quadrant, indicating they are relatively cool yet brighter than average. Ascertaining fire properties between the lower right and upper left quadrants is difficult for the reasons mentioned earlier. Finally, 11% of fire pixels are in the lower left quadrant, indicating they are cool and dim. Pixels in this quadrant either have low fire fractions or low temperatures, which could mean they are young and/or expiring hotspots. The specific thresholds used to divide these four quadrants and our hypotheses need to be further studied, but the data from this paper suggest that a combination of DNB and MWIR data [as shown in Fig. 6(b)] adds more information to characterize the life cycle of a fire event as well as the characteristics of each fire pixel, both of which have implications for studying fire dynamics, fire weather, and fire emissions. Indeed, the correlation between BT_4 (the fire pixel energy) and DNB is relatively high [0.69, see Fig. 6(b)], suggesting the utility of FILDA for detecting nighttime fires. The time series of the mean DNB radiance and BT_4 for all FILDA pixels of all aggregation zones shows a correlation of 0.69; both have progressively smaller radiances and temperatures toward the end of the Rim Fire event. This contrast of DNB radiances during the lifetime of the Rim Fire is more significant than the contrast of mean BT_4 s for fire pixels, suggesting the further need to use the DNB alongside NIR and MWIR data to characterize fire events.

The algorithm is also evaluated by studying the Rim Fire on 24 August 2013, which had a near-coincident ASTER overpass. The Rim Fire was imaged the night immediately after its second day of explosive growth, during which it doubled its area burned from the day before. The explosive growth left large swaths of smoldering vegetation in its wake. Fig. 7 shows a multiband view of the Rim Fire that night, as well as the ASTER imagery. Fig. 7(a) shows the pixel locations overlaid onto Google Earth satellite imagery. The blue boxes represent FILDA pixels, whereas the green boxes are the AFARP pixel locations. In this scene, every AFARP pixel is also independently identified as a FILDA pixel (gold boxes). The rest of the panels (b)–(e) show the Rim Fire at different wavelengths. On the VIIRS BT_4 map [see Fig. 7(b)], the fire front is easily discernible. AFARP captures the most intense fire hotspots, but much of it is ignored. FILDA, on the other hand, shows a more continuous fire front. ASTER's $8.3\text{-}\mu\text{m}$ band [see Fig. 7(c)], showing the fire front hot spots at a much finer resolution, was

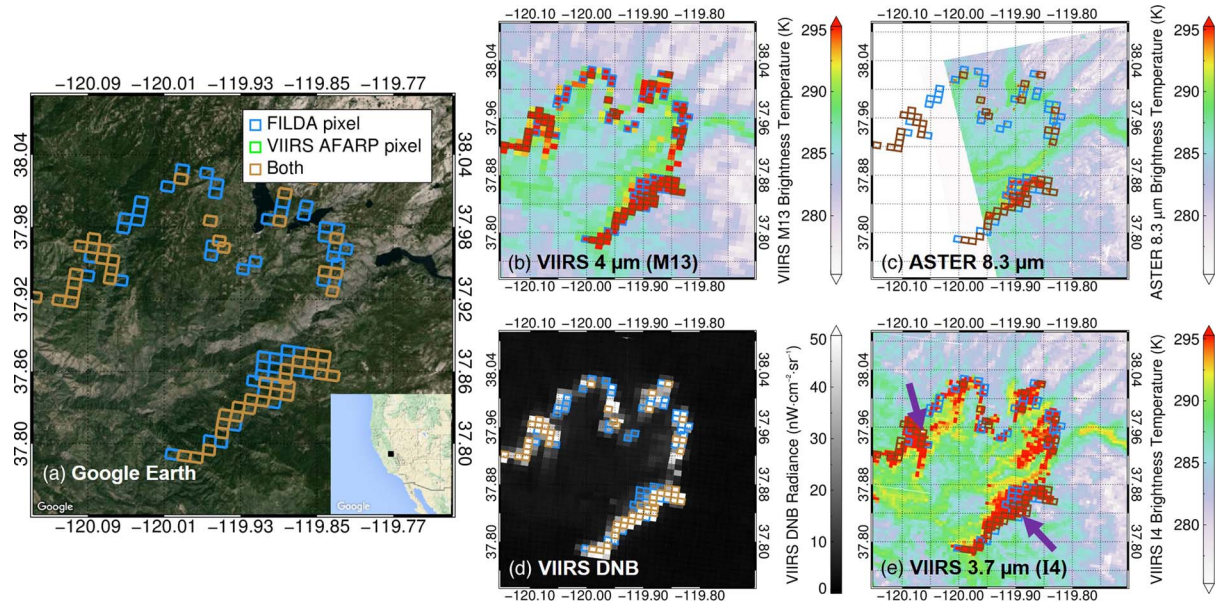


Fig. 7. Multiband/sensor view of the Rim Fire taken at 2:29 A.M. PDT on 24 August 2013 by VIIRS. ASTER [panel (c)], aboard Terra, scanned the fire at 11:01 P.M. PDT on 23 August 2013. The blue boxes are pixels detected by FILDA, whereas the gold boxes are classified as fires by FILDA and AFARP. Note that FILDA also included all AFARP pixels. The purple arrows in (e) point to saturating pixels in the I4 band.

imaged 3.5 h before VIIRS. While the ASTER band shows a tendency to slightly emphasize smoldering terrain, the fire front is still well colocated with the VIIRS fire pixel footprints. It also reminds us that fire events are entirely subpixel in nature, even in large fire complexes such as this Rim Fire scene. The DNB image [see Fig. 7 (d)] suggests two important points: 1) It is correlated with the $4\text{ }\mu\text{m}$ band; and 2) it is useful for identifying weakly burning terrain (some of which is even identified as fire pixels by FILDA). Finally, the VIIRS I4 band (centered at $3.7\text{ }\mu\text{m}$) is shown in Fig. 7(e). The increased spatial resolution highlights the terrain effects and smaller flare-ups not well observed in the moderate-resolution $4\text{ }\mu\text{m}$ band. Unfortunately, there are two I4 pixels that saturate in this scene and appear as missing data. They have been marked with the two purple arrows as they are hard to identify.

The VIIRS 24 August 2013 scene is further analyzed to show the method by which FILDA operates. A 2-D histogram of DNB radiances versus $4\text{-}\mu\text{m}$ BTs for the entire granule is presented in Fig. 8, binned into increments of $1\text{ nW}\cdot\text{cm}^{-2}\cdot\text{sr}^{-1}$ (DNB) and 1 K BTs ($4\text{ }\mu\text{m}$). It shows which pixels are classified as fires by FILDA and AFARP. The dashed gold line indicates the $4\text{-}\mu\text{m}$ potential fire pixel BT threshold of 305 K used by AFARP and by FILDA when the DNB radiance is below the minimum DNB threshold. The solid blue line represents the threshold determined by FILDA. In this case, the BT_4 threshold is 298 K , and the DNB threshold is $12\text{ nW}\cdot\text{cm}^{-2}\cdot\text{sr}^{-1}$. Importantly, AFARP does not classify many of the potential fire pixels as fires, whereas FILDA does. There is no publicly available diagnostic information for AFARP; therefore, there is no method of identifying why and how the pixels are disqualified as fires. Second, there are many fire pixels with BTs less than 305 K , highlighting the need for reduced thresholds (preferably dynamically as in FILDA). Other case studies will show how the BT and DNB distributions change for each scene.

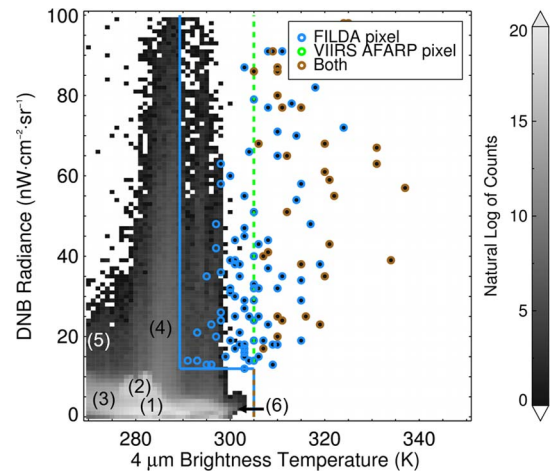


Fig. 8. Two-dimensional histogram of the Rim Fire VIIRS granule used in Fig. 7, showing fire pixel classifications for both FILDA and AFARP. In this case, every AFARP pixel is also a FILDA pixel. The blue line represents the FILDA thresholds, whereas the gold dashed line is the AFARP threshold. The annotated numbers describe each population of pixels: 1) most low-altitude terrain and open Pacific Ocean pixels; 2) marine stratus clouds; 3) high altitude terrain, cirrus clouds, and some cooler marine stratus clouds; 4) nonarid cities and towns, warm marine stratus clouds; 5) cities under partial cloud cover; and 6) desert environments.

Several different populations of pixels are visible in Fig. 8, marked by different numbers. They are presented as follows with decreasing occurrence. The major population in group (1) is comprised of low-altitude terrain, which reflects some moonlight, and then open Pacific Ocean water, which represents the lowest bins under the label (1). Group (2) represents the majority of marine stratus clouds. Group (3) consists of a variety of features, which include high-altitude terrain such as the Sierra Nevada Mountain Range and ranges in western Nevada and Central Oregon. It also contains pixels adjacent to

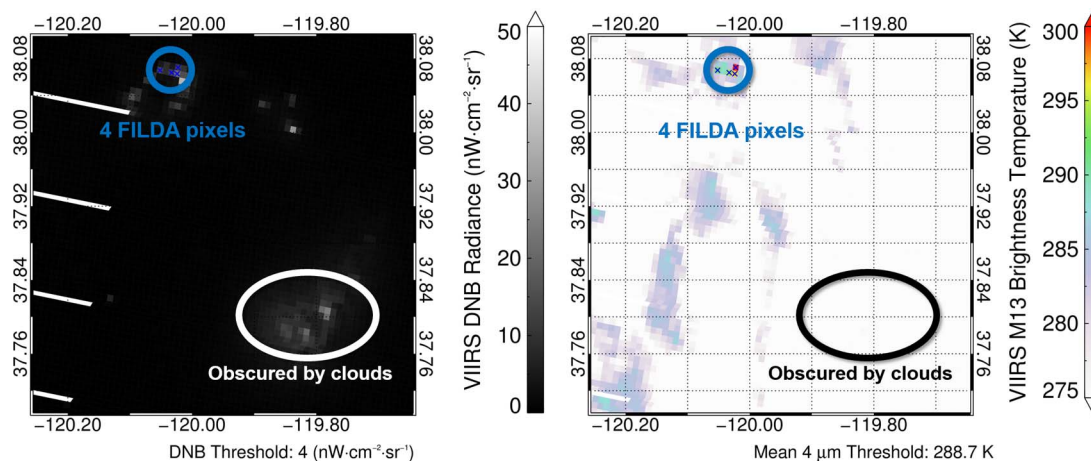


Fig. 9. Imagery from 3 September 2013 showing the Rim Fire still burning underneath the cloud cover. AFARP could not identify any pixels but FILDA identified four.

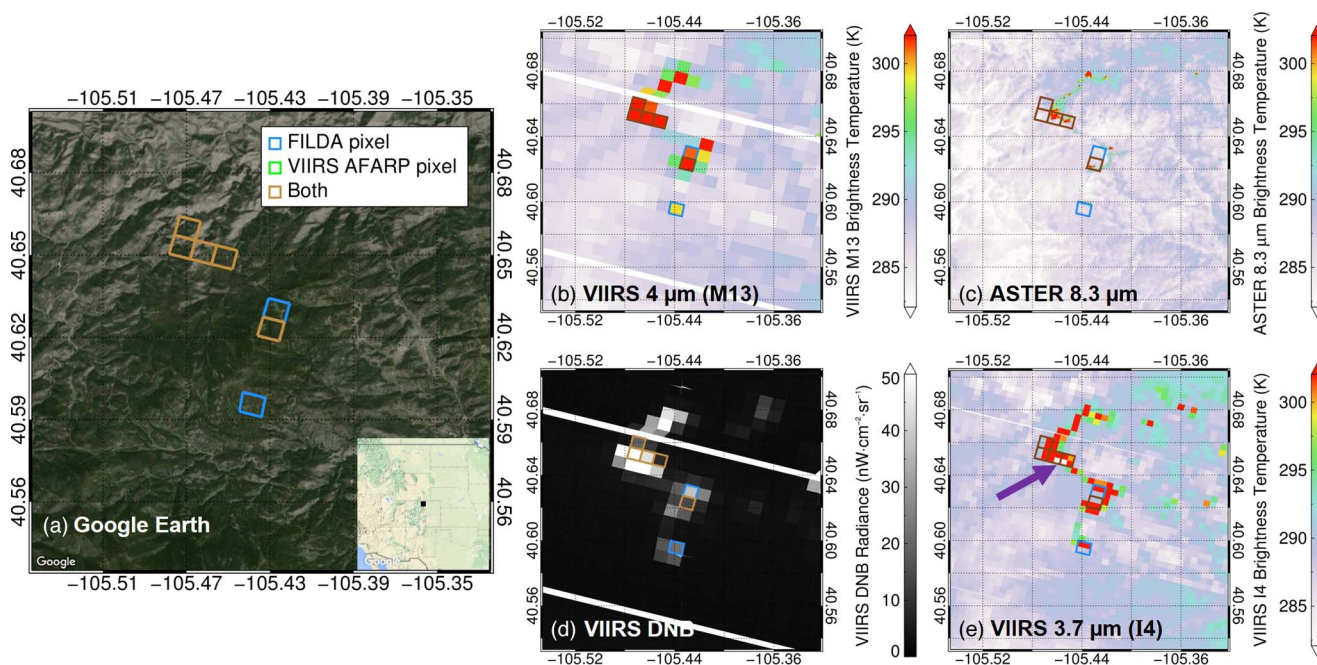


Fig. 10. Multiband/sensor view of the High Park fire taken at 3:04 A.M. MDT on 19 June 2012 by VIIRS. ASTER [panel (c)] scanned the fire at 11:05 P.M. MDT on 18 June 2012. The blue boxes are pixels detected by FILDA, whereas the green boxes are AFARP detections. Note that FILDA also included all AFARP pixels (gold boxes). The purple arrow in (e) points to saturating pixels in the I4 band.

higher clouds. Finally, some of the cooler marine stratus clouds are in this population. Group (4) varies widely in spatial distribution, but pixels are mostly nonarid locations such as cities like San Francisco and smaller towns. There are some highly reflective marine stratus clouds in this population as well, but it is primarily dominated by artificial lights. Conversely, group (5) is relatively uncommon and contains partially cloud-covered cities; the visible light penetrates the clouds, but the clouds are attenuating the $4\text{ }\mu\text{m}$ signal. Finally, an unusual group (6) exists only in very warm areas. In this scene, only two places belong in this group: Death Valley and the waters of the Salton Sea, both located in Southern California. Although not marked as a specific group, fires can be seen as the outliers in warmer BTs and brighter DNB values.

During the course of the Rim Fire, there were several periods of cloud cover from pyroconvection and frontal passages. Unsurprisingly, during those times, AFARP has trouble identifying

fire pixels because of the attenuated fire signal in the $4\text{-}\mu\text{m}$ channel. The issue is further compounded by cloud cover reducing solar heating during the day, and when combined with an arbitrarily high potential fire pixel threshold, makes fires particularly challenging to detect. Cloud cover moving into the area on 3 September 2013 is one such case (see Fig. 9). AFARP is unable to detect any fire pixels, but despite the less-than-favorable conditions, the Rim Fire can still be seen burning underneath the cloud cover. Similarly, FILDA is unable to see the fires burning beneath the clouds, but it is able to identify four fire pixels on the periphery of the cloud edge due to the reduced (mean) BT_4 threshold of 288.7 K .

While the Rim Fire was a devastating fire, it provided the perfect opportunity to test FILDA and examine AFARP's performance due to its long burn duration and intense nighttime activity. In the remaining examples, we investigate a variety of other fires and apply FILDA to them.

B. High Park Fire

On 9 June 2012, lightning ignited a fire in the Roosevelt National Forest, near Fort Collins, Colorado (<http://inciweb.nwcg.gov/incident/2904/>). The fire burned for ~ 21 days and scorched 87 000 acres before it was declared 100% contained on 30 June 2012. As the fire was located near Fort Collins, over 250 homes were destroyed, causing estimated damage and suppression costs of \$39.2 million. Like the Rim Fire, it was a high-impact fire that burned intensely in excess of two weeks, making it another ideal candidate for FILDA. Here, we only examine one day of observations, and not all of the observations over the course of the wildfire's lifespan.

The investigated nighttime period is 19 June 2012 primarily because that evening had a near-coincident ASTER overpass [see Fig. 10(c)]. ASTER scanned the fire event at 11:05 P.M. MDT on 18 June, with VIIRS overpassing the fire at 3:04 A.M. MDT on 19 June. Although the 4-h difference is significant, the High Park fire did not spread substantially during that period, and the same hot spots are still visible with both ASTER and VIIRS. FILDA identifies an intense hot spot that AFARP neglected: the southernmost portions of the fire (see Fig. 10). Instead, AFARP only flags the central portion of the fire front, highlighting potential for improvement even with fires of moderate intensity.

The reason behind its difficulty with detecting those fires is easily discernible in Fig. 11. With AFARP's minimum BT_4 threshold of 305 K, the majority of fire pixels are discarded before any analysis is done (e.g., anything to the left of the dashed green line). To the contrary, FILDA determines that the minimum BT_4 threshold should be 294 K for the High Park fire potential pixels, which encompasses these missed hot spots while successfully excluding the nonfire pixels. However, even FILDA does not classify some of these obvious hot spots as fires because they either fail the background tests or have a $\Delta BT < 10$ K, showing the difficulty of fine-tuning fire detection algorithms. To reiterate, the solid blue line at 289 K in Fig. 11 is the mean BT_4 threshold for the entire granule, also encompassing fire complexes burning in the mountains of Idaho and Colorado. The outlying fire detection at 290 K is a gas flare in central Alberta (hence the low threshold), which will be discussed next.

C. Gas Flares

One unintended but important application of FILDA involves the detection of gas flares. While other algorithms exist for the sole purpose of flare detection and characterization using other satellite platforms (e.g., in [69] and [70]) or use fundamentally different parts of the IR spectrum (as in [63]), FILDA shows potential for nocturnal gas flaring detection based on the reduction of the BT_4 threshold. Two gas-flaring regions are examined. First, the Khanty-Mansiysk region of Russia is examined because of its rapid development in recent years and its high volume of flared gas. Second, offshore flares in the Niger Delta are investigated in order to test FILDA's potential for monitoring flares over open water.

Although gas flares do not pose a direct risk to life and property, they do emit hazardous compounds as by-products

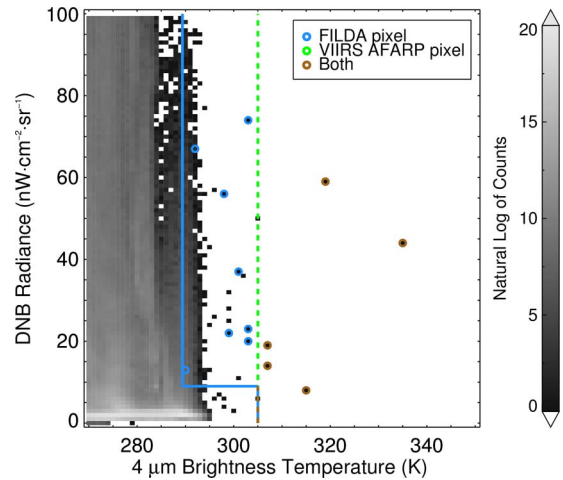


Fig. 11. Two-dimensional histogram of the granule used in Fig. 10 showing fire pixel classifications for both FILDA and AFARP. As in Fig. 8, blue circles indicate FILDA fire pixels, whereas the green circles are AFARP detections. The solid blue line represents FILDA's DNB and mean BT_4 threshold, whereas the gold dashed line is the 305 K $4 \mu\text{m}$ BT potential fire pixel threshold used by AFARP (and FILDA with little light). It should be noted that this scatter plot includes the entire granule and not just the region shown in the previous figure.

of incomplete combustion. These include soot, partially combusted hydrocarbons, CO, CO₂, NO_x, and SO₂ [71]. Unfortunately, it is often difficult to obtain flare volume and location information from their operators due to security concerns and lack of accountability, particularly in poorer countries [70]. Remote sensing fills that important void in the estimation of gas flaring emission impacts.

Located in Central Russia, Khanty-Mansi is an oil producing region that has been growing rapidly in the last two decades. In 2011, it constituted 51.3% of Russia's oil production and continues to increase [72]. A very small portion of the region is shown in Fig. 12. Fig. 12(a) shows a portion of the flare complex located near the Ob River; notice in the center of the image, there is a FILDA detection over what is seemingly wilderness. Recent higher-resolution imagery available through Google Earth (not shown) indicates human activity at the location of the hot spot. The flare signatures are two flow stations, which are structures that collect natural gas from smaller wells and flare them in a centralized location. In Fig. 12, the flare signature is visible in all bands, although the DNB highlights the feature exceptionally well. Unfortunately, the BT_4 threshold in AFARP is too high to consider them as potential fire pixels.

The Niger Delta, like the Khanty-Mansi region, is also home to large-scale oil and gas production. The region is infamous for the ecological devastation that petroleum extraction has wreaked on its fragile estuarial ecosystems [73] which include large mangroves. Nigeria was reportedly flaring 99% of its natural gas production as recently as 2003 [74], but laws passed in recent years banning the practice have reduced the portion of gas flared to under 20% [75]. Field studies are rarely conducted, and most flaring estimates are derived from satellite data, such as in [70].

While both AFARP and FILDA are able to identify large flow stations on land (FILDA improves detection of smaller sources), offshore oil rig flares are not identified by AFARP

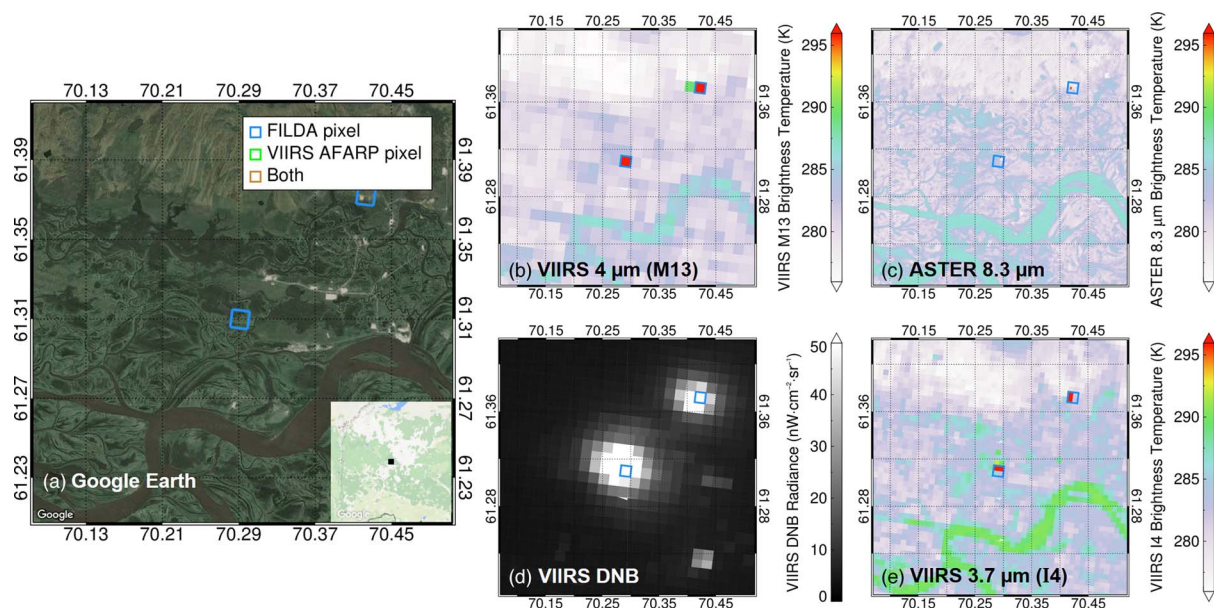


Fig. 12. Multiband/sensor view of two gas flares in the Khanti-Mansiysk region of Russia from 20:52 UTC (2:52 A.M. local time) on 9 August 2013 by VIIRS. ASTER [panel (c)] scanned the flares at 16:44 UTC (10:44 P.M. local time). The blue boxes are pixels detected by FILDA (AFARP omitted both flares). The BT_4 threshold is 287 K, and the DNB threshold is 6 $\text{nW}/\text{cm}^2\text{-sr}$.

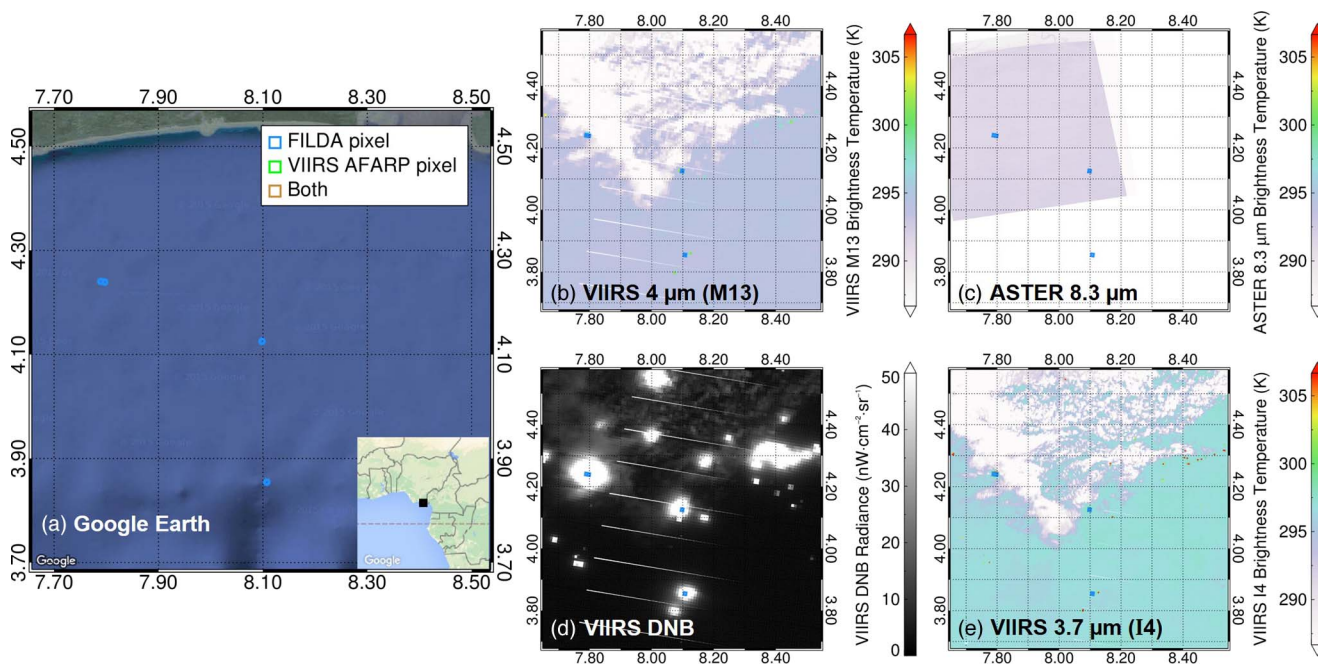


Fig. 13. Multiband/sensor views of offshore gas flares by VIIRS and ASTER, using the same 01:20:47 UTC 19 December 2013 VIIRS granule as in Table II. Larger flares are identified by FILDA, but smaller flares are still omitted. The ASTER overpass time was 21:55:58 UTC on 18 December 2013.

because all water pixels are initially screened out by the algorithm to avoid false positives associated with daytime sun glint. With the inclusion of water pixels, offshore rigs are easily identified. Using the VIIRS scene from 01:20:47 UTC on 19 December 2013, overlooking parts of the Niger Delta and Southern Atlantic, flares stand out from the background with both the DNB and M13. Table II shows the detections of the granule and their associated information. Of particular note is that most of these offshore flares listed in the table are extremely hot and bright, and even well above the minimum

detection threshold for AFARP. Fig. 13 shows some of these flare detections, with hot spots apparent in every band. Unfortunately, many of the smaller flares that can be seen in the DNB image [see Fig. 13(d)] are not detected by FILDA. Some flares are omitted because their BT_4 signatures are masked by overlying marine stratus clouds, despite their visible DNB signatures. Other flares are omitted because they are smaller and their ΔBT signatures are less than 10 K. The I4 band does, however, highlight many of these smaller hot spots; this feature might be useful to include in future refinements, as it

TABLE II
OFFSHORE FLARE CHARACTERISTICS FROM THE 01:20:47 UTC
19 DECEMBER 2013 VIIRS GRANULE AS DETECTED BY FILDA. THE
MEAN BT_4 THRESHOLD IS 294.7 K, AND THE DNB
THRESHOLD IS $20 \text{ nW} \cdot \text{cm}^{-2} \cdot \text{sr}^{-1}$

Lat. (°)	Lon. (°)	BT_4 (K)	BT_{11} (K)	DNB ($\text{nW} \cdot \text{cm}^{-2} \cdot \text{sr}^{-1}$)
5.35	4.34	318.90	297.63	1378.4
4.66	6.07	306.45	291.80	1571.5
4.24	7.78	325.39	291.12	5911.9
4.23	7.79	348.84	294.31	3455.1
4.12	8.09	317.51	294.95	3988.3
4.13	7.51	317.76	295.08	4437.0
4.13	7.52	306.04	294.78	2191.4
4.55	4.61	304.37	293.71	1432.8
3.99	7.28	305.89	295.21	3523.2
3.98	7.29	323.75	295.82	10294.5
3.85	8.10	308.99	294.92	5426.8
3.57	7.39	331.31	296.45	9777.5
1.40	9.23	311.29	293.35	4372.1
-1.52	9.94	303.87	288.29	164.8

is colocated with the M-bands. Despite missing these smaller flares, FILDA, unlike AFARP, detects larger flares and works over open water.

VI. CONCLUSION

This paper has presented a novel approach to detecting wild-fires, biomass burning, and gas flares at night by incorporating visible light into the fire detection algorithm. Although Croft proposed the idea over 40 years ago [20], the fire algorithms developed since then utilize only the IR portion of the electromagnetic spectrum. Due to the launch of VIIRS in October of 2011 with its DNB, we are finally able to incorporate visible data into these algorithms to further refine them. FILDA is the result of this approach. Our approach is based on the official VIIRS IDPS fire product algorithm, known as the AFARP, with modifications to improve the detection of low temperature hotspots. We recognize that AFARP is based on a dated algorithm and is different from the other two recently available VIIRS-based fire products generated respectively as part of the NDE system (operational since early 2016) and NASA's production systems. Indeed, other fire detection algorithms utilizing VIIRS have already shown much potential; for example, Schroeder *et al.* [17] have made progress in developing an operational algorithm using the 375-m resolution I-bands, and Elvidge *et al.* [63] developed a nocturnal gas flare detection algorithm based on 1.6- μm and other IR bands that also retrieves subpixel fire characteristics. However, our modifications to AFARP are due to two primary considerations: 1) the 375-m fire product does not currently permit quantitative FRP retrieval [17], thus improving the sensitivity of the 750 m algorithm is meaningful; and 2) by combining the DNB and IR bands, FILDA has the theoretical potential to distinguish between flaming and smoldering phases, thereby improving emission factor estimates for fire emission models. By definition, if a pixel is hot and emits light at night, the fire in that pixel should

have a flaming component; in contrast, if a pixel is hot and emits no light, the fire in that pixel is likely in the smoldering phase.

Many case studies (including those not presented here) show that FILDA has potential in improving the detection of wild-fires. Overall, the number of FILDA detections nearly doubles that of AFARP. This mainly occurs at the fringes of fire fronts and the weakly burning terrain left in their wake where the BT_4 s were slightly under AFARP detection thresholds. Both FILDA and AFARP still miss most smoldering fires, characterized by lower burning temperatures and low visible light output. Errors of commission were rare and primarily confined to large industrial complexes (such as steel mills). In addition to wildfires, FILDA improves the detection of gas flares. Although significant numbers of small flares are still omitted by FILDA because of their weak IR signatures, many more flow stations are observed than in AFARP. One marked improvement is with the detection of offshore oil rig flares since FILDA does not prescreen water pixels from the selection of potential fire pixels.

Of particular note is the power FILDA has for detecting smaller and cooler fires that would otherwise be omitted from detection by AFARP. The Rim Fire in California is a good example of this; FILDA is able to identify the fire the first night it burned, whereas AFARP required an additional day for the Rim Fire pixels to reach detection thresholds. This has broad implications for the fire response and management community, since earlier response is paramount to controlling fires while they are still manageable. Further refinement of this approach (with possible combined use of data from GOES) could lead to earlier detection of fires in both clear and cloudy conditions over various surface types, reducing fire-related property damage and loss of life. Given many fires in remote regions are caused by lightning [76], more studies are needed for evaluating the potential of using the DNB together with IR data from VIIRS and GOES to detect fires near cloud edges at night.

REFERENCES

- [1] A. L. Westerling, H. G. Hidalgo, D. R. Cayan, and T. W. Swetnam, "Warming and earlier spring increase western US forest wildfire activity," *Science*, vol. 313, no. 5789, pp. 940–943, Aug. 18, 2006, doi: 10.1126/science.1128834.
- [2] K. Haynes, J. Handmer, J. McAneney, A. Tibbits, and L. Coates, "Australian bushfire fatalities 1900–2008: Exploring trends in relation to the 'prepare, stay and defend or leave early' policy," *Environ. Sci. Policy*, vol. 13, no. 3, pp. 185–194, May 2010, doi: 10.1016/j.envsci.2010.03.002.
- [3] National Interagency Fire Center, *Federal Firefighting Costs (Suppression Only)*, 2015. [Online]. Available: https://www.nifc.gov/fireInfo/fireInfo_documents/SuppCosts.pdf
- [4] M. Re, *Wildfires*, 2015. [Online]. Available: <http://www.iii.org/fact-statistic/wildfires>
- [5] W. M. Hao, D. E. Ward, G. Olbu, and S. P. Baker, "Emissions of CO₂, CO, and hydrocarbons from fires in diverse African savanna ecosystems," *J. Geophys. Res.-Atmos.*, vol. 101, no. D19, pp. 23 577–23 584, Oct. 30, 1996, doi: 10.1029/95JD02198.
- [6] C. Ichoku and Y. J. Kaufman, "A method to derive smoke emission rates from MODIS fire radiative energy measurements," *IEEE Trans. Geosci. Remote Sens.*, vol. 43, no. 11, pp. 2636–2649, Nov. 2005, doi: 10.1109/TGRS.2005.857328.
- [7] J. Wang *et al.*, "Mesoscale modeling of Central American smoke transport to the united states: 1. 'top-down' assessment of emission strength and diurnal variation impacts," *J. Geophys. Res.-Atmos.*, vol. 111, no. D5, Mar. 9, 2006, Art. no. D05S17, doi: 10.1029/2005JD006416.
- [8] T. J. Duck *et al.*, "Transport of forest fire emissions from Alaska and the Yukon territory to nova scotia during summer 2004," *J. Geophys. Res.-Atmos.*, vol. 112, no. D10, May 19, 2007, Art. no. D10S44, doi: 10.1029/2006JD007716.

- [9] G. R. van der Werf *et al.*, "Global fire emissions and the contribution of deforestation, savanna, forest, agricultural, and peat fires (1997–2009)," *Atmos. Chem. Phys.*, vol. 10, no. 23, pp. 11 707–11 735, 2010, doi: 10.5194/acp-10-11707-2010.
- [10] D. L. Westphal and O. B. Toon, "Simulations of microphysical, radiative, and dynamic processes in a continental-scale forest-fire smoke plume," *J. Geophys. Res.-Atmos.*, vol. 96, no. D12, pp. 22 379–22 400, Dec. 20, 1991, doi: 10.1029/91JD01956.
- [11] Y. J. Kaufman *et al.*, "Passive remote sensing of tropospheric aerosol and atmospheric correction for the aerosol effect," *J. Geophys. Res.-Atmos.*, vol. 102, no. D14, pp. 16 815–16 830, Jul. 27, 1997, doi: 10.1029/97JD01496.
- [12] Y. J. Kaufman, D. Tanre, and O. Boucher, "A satellite view of aerosols in the climate system," *Nature*, vol. 419, no. 6903, pp. 215–223, Sep. 12, 2002, doi: 10.1038/nature01091.
- [13] V. Ramanathan *et al.*, "Indian ocean experiment: An integrated analysis of the climate forcing and effects of the great Indo-Asian haze," *J. Geophys. Res.-Atmos.*, vol. 106, no. D22, pp. 28 371–28 398, Nov. 27, 2001, doi: 10.1029/2001JD000133.
- [14] O. Dubovik *et al.*, "Single-scattering albedo of smoke retrieved from the sky radiance and solar transmittance measured from ground," *J. Geophys. Res.-Atmos.*, vol. 103, no. D24, pp. 31 903–31 923, Dec. 27, 1998, doi: 10.1029/98JD02276.
- [15] S. P. Flasse *et al.*, "Warming and earlier spring increase western US forest wildfire activity," *Science*, vol. 313, no. 5789, pp. 940–943, 2006.
- [16] D. K. Davies, S. Ilavajhala, M. M. Wong, and C. O. Justice, "Fire information for resource management system: Archiving and distributing modis active fire data," *IEEE Trans. Geosci. Remote Sens.*, vol. 47, no. 1, pp. 72–79, Jan. 2009, doi: 10.1109/TGRS.2008.2002076.
- [17] W. Schroeder, P. Oliva, L. Giglio, and I. A. Csizsar, "The new VIIRS 375 m active fire detection data product: Algorithm description and initial assessment," *Remote Sens. Environ.*, vol. 143, pp. 85–96, Mar. 5, 2014, doi: 10.1016/j.rse.2013.12.008.
- [18] C. Elvidge *et al.*, "Radiance calibration of DMSP-OLS low-light imaging data of human settlements," *Remote Sens. Environ.*, vol. 68, no. 1, pp. 77–88, Apr. 1999, doi: 10.1016/S0034-4257(98)00098-4.
- [19] L. G. Dickinson, S. E. Bosely, III, and W. S. Burgmann, "Defense Meteorological Satellite Program (DMSP) user's guide," Air Weather Service, U.S. Air Force, Washington, DC, USA, Dec. 1974.
- [20] T. A. Croft, "Burning waste gas in oil fields," *Nature*, vol. 245, no. 5425, pp. 375–376, Oct. 1973, doi: 10.1038/245375a0.
- [21] T. A. Croft, "Nighttime images of the earth from space," *Sci. Amer.*, vol. 239, pp. 86–98, 1978, doi: 10.1038/scientificamerican0778-86.
- [22] R. Welch, "Monitoring urban-population and energy-utilization patterns from satellite data," *Remote Sens. Environ.*, vol. 9, no. 1, pp. 1–9, 1980, doi: 10.1016/0034-4257(80)90043-7.
- [23] C. D. Elvidge *et al.*, *Algorithm for the Retrieval of Fire Pixels From DMSP Operational Linescan System*. Cambridge, MA, USA: MIT Press, 1996, ch. 8, pp. 73–85.
- [24] C. Elvidge, K. Baugh, E. Kihn, H. Kroehl, and E. Davis, "Mapping city lights with nighttime data from the DMSP operational linescan system," *Photogramm. Eng. Remote Sens.*, vol. 63, no. 6, pp. 727–734, Jun. 1997.
- [25] D. A. Hastings and W. J. Emery, "The advanced very high-resolution radiometer (AVHRR)—A brief reference guide," *Photogramm. Eng. Remote Sens.*, vol. 58, no. 8, pp. 1183–1188, Aug. 1992.
- [26] J. Dozier, "A method for satellite identification of surface-temperature fields of subpixel resolution," *Remote Sens. Environ.*, vol. 11, no. 3, pp. 221–229, 1981, doi: 10.1016/0034-4257(81)90021-3.
- [27] M. Matson and J. Dozier, "Identification of subresolution high-temperature sources using a thermal IR sensor," *Photogramm. Eng. Remote Sens.*, vol. 47, no. 9, pp. 1311–1318, Sep. 1981.
- [28] J. M. Lobert and J. Warnatz, *Emissions From the Combustion Process in Vegetation*, vol. 13. New York, NY, USA: Wiley, 1993, pp. 15–37.
- [29] L. Giglio and J. D. Kendall, "Application of the dozier retrieval to wildfire characterization—A sensitivity analysis," *Remote Sens. Environ.*, vol. 77, no. 1, pp. 34–49, Jul. 2001, doi: 10.1016/S0034-4257(01)00192-4.
- [30] M. Flannigan and T. Vonderhaar, "Forest-fire monitoring using NOAA satellite AVHRR," *Can. J. Forest Res.-Revue Canadienne De Recherche Forestiere*, vol. 16, no. 5, pp. 975–982, Oct. 1986, doi: 10.1139/x86-171.
- [31] J. Robinson, "Fire from space—Global fire evaluation using infrared remote-sensing," *Int. J. Remote Sens.*, vol. 12, no. 1, pp. 3–24, Jan. 1991.
- [32] E. Prins, J. Feltz, W. Menzel, and D. Ward, "An overview of goes-8 diurnal fire and smoke results for SCAR-B and 1995 fire season in south america," *J. Geophys. Res.-Atmos.*, vol. 103, no. D24, pp. 31 821–31 835, Dec. 27, 1998.
- [33] E. Prins and W. Menzel, "Geostationary satellite detection of biomass burning in South-America," *Int. J. Remote Sens.*, vol. 13, no. 15, pp. 2783–2799, Oct. 1992.
- [34] C. Justice *et al.*, "The MODIS fire products," *Remote Sens. Environ.*, vol. 83, no. 1/2, pp. 244–262, Nov. 2002, doi: 10.1016/S0034-4257(02)00076-7.
- [35] L. Giglio, J. Descloitres, C. O. Justice, and Y. J. Kaufman, "An enhanced contextual fire detection algorithm for MODIS," *Remote Sens. Environ.*, vol. 87, no. 2/3, pp. 273–282, Oct. 15, 2003, doi: 10.1016/S0034-4257(03)00184-6.
- [36] I. Csizsar *et al.*, "Active fires from the Suomi NPP visible infrared imaging radiometer suite: Product status and first evaluation results," *J. Geophys. Res., Atmos.*, vol. 119, no. 2, pp. 85–96, 2013, doi: 10.1016/j.rse.2013.12.008.
- [37] D. Peterson, J. Wang, C. Ichoku, E. Hyer, and V. Ambrosia, "A sub-pixel-based calculation of fire radiative power from modis observations: 1 algorithm development and initial assessment," *Remote Sens. Environ.*, vol. 129, pp. 262–279, Feb. 15, 2013, doi: 10.1016/j.rse.2012.10.036.
- [38] S. Flasse and P. Ceccato, "A contextual algorithm for AVHRR fire detection," *Int. J. Remote Sens.*, vol. 17, no. 2, pp. 419–424, Jan. 20, 1996.
- [39] O. Arino and J. M. Melinotte, "The 1993 Africa fire map," *Int. J. Remote Sens.*, vol. 19, no. 11, pp. 2019–2023, Jul. 20, 1998, doi: 10.1080/014311698214839.
- [40] C. O. Justice, J. D. Kendall, P. R. Dowty, and R. J. Scholes, "Satellite remote sensing of fires during the safari campaign using NOAA advanced very high resolution radiometer," *J. Geophys. Res.-Atmos.*, vol. 101, no. D19, pp. 23 851–23 863, Oct. 30, 1996, doi: 10.1029/95JD00623.
- [41] Z. Li *et al.*, *A Review of AVHRR-Based Active Fire Detection Algorithms: Principles, Limitations, and Recommendations*. Hague, The Netherlands: SPB Academic, 2001.
- [42] L. Giglio and J. D. Kendall, "Evaluation of global fire detection algorithms using simulated AVHRR infrared data," *Int. J. Remote Sens.*, vol. 20, no. 10, pp. 1947–1985, Jul. 10, 1999, doi: 10.1080/014311699212290.
- [43] M. Matson and B. Holben, "Satellite detection of tropical burning in brazil," *Int. J. Remote Sens.*, vol. 8, no. 3, pp. 509–516, Mar. 1987.
- [44] E. Prins and W. Menzel, "Trends in South-American biomass burning detected with the goes visible infrared spin scan radiometer atmospheric sounder from 1983 to 1991," *J. Geophys. Res.-Atmos.*, vol. 99, no. D8, pp. 16 719–16 735, Aug. 20, 1994.
- [45] J. S. Reid *et al.*, "Global monitoring and forecasting of biomass-burning smoke: Description of and lessons from the fire locating and modeling of burning emissions (flambe) program," *IEEE J. Sel. Topics Appl. Earth Observ. Remote Sens.*, vol. 2, no. 3, pp. 144–162, Sep. 2009, doi: 10.1109/JSTARS.2009.2027443.
- [46] Y. J. Kaufman, R. G. Kleidman, and M. D. King, "SCAR-B fires in the tropics: Properties and remote sensing from EOS-MODIS," *J. Geophys. Res.-Atmos.*, vol. 103, no. D24, pp. 31 955–31 968, Dec. 27, 1998, doi: 10.1029/98JD02460.
- [47] Y. J. Kaufman *et al.*, "Potential global fire monitoring from EOS-MODIS," *J. Geophys. Res.-Atmos.*, vol. 103, no. D24, pp. 32 215–32 238, Dec. 27, 1998, doi: 10.1029/98JD01644.
- [48] C. Ichoku, L. Giglio, M. J. Wooster, and L. A. Remer, "Global characterization of biomass-burning patterns using satellite measurements of fire radiative energy," *Remote Sens. Environ.*, vol. 112, no. 6, pp. 2950–2962, Jun. 16, 2008, doi: 10.1016/j.rse.2008.02.009.
- [49] D. Peterson and J. Wang, "A sub-pixel-based calculation of fire radiative power from modis observations: 2. Sensitivity analysis and potential fire weather application," *Remote Sens. Environ.*, vol. 129, pp. 231–249, Feb. 15, 2013, doi: 10.1016/j.rse.2012.10.020.
- [50] C. Cao, F. J. D. Luccia, X. Xiong, R. Wolfe, and F. Weng, "Early on-orbit performance of the visible infrared imaging radiometer suite onboard the Suomi National Polar-Orbiting Partnership (S-NPP) satellite," *IEEE Trans. Geosci. Remote Sens.*, vol. 52, no. 2, pp. 1142–1156, Feb. 2014, doi: 10.1109/TGRS.2013.2247768.
- [51] R. E. Wolfe *et al.*, "Suomi NPP VIIRS prelaunch and on-orbit geometric calibration and characterization," *J. Geophys. Res.-Atmos.*, vol. 118, no. 20, Oct. 27, 2013, doi: 10.1002/jgrd.50873.
- [52] D. Hillger *et al.*, "First-light imagery from suomi NPP VIIRS," *Bull. Amer. Meteorol. Soc.*, vol. 94, no. 7, pp. 1019–1029, Jul. 2013, doi: 10.1175/BAMS-D-12-00097.1.
- [53] T. N. Polivka, E. J. Hyer, J. Wang, and D. A. Peterson, "First global analysis of saturation artifacts in the VIIRS infrared channels and the effects of sample aggregation," *IEEE Geosci. Remote Sens. Lett.*, vol. 12, no. 6, pp. 1262–1266, Jun. 2015, doi: 10.1109/LGRS.2015.2392098.
- [54] S. Miller, S. Haddock, C. Elvidge, and T. Lee, "Detection of a bioluminescent milky sea from space," *Proc. Nat. Acad. Sci. United*

- States Amer.*, vol. 102, no. 40, pp. 14 181–14 184, Oct. 4, 2005, doi: 10.1073/pnas.0507253102.
- [55] T. E. Lee *et al.*, “The NPOESS VIIRS day/night visible sensor,” *Bull. Amer. Meteorol. Soc.*, vol. 87, no. 2, pp. 191–199, 2006, doi: 10.1175/BAMS-87-2-191. [Online]. Available: <http://0-search.ebscohost.com.library.unl.edu/login.aspx?direct=true&db=aph&AN=19897069&site=ehost-live>
- [56] S. D. Miller *et al.*, “Suomi satellite brings to light a unique frontier of nighttime environmental sensing capabilities,” *Proc. Nat. Acad. Sci. United States Amer.*, vol. 109, no. 39, pp. 15 706–15 711, Sep. 25, 2012, doi: 10.1073/pnas.1207034109.
- [57] L. B. Liao, S. Weiss, S. Mills, and B. Hauss, “Suomi NPP VIIRS day–night band on-orbit performance,” *J. Geophys. Res.-Atmos.*, vol. 118, no. 22, pp. 12 705–12 718, Nov. 27, 2013, doi: 10.1002/2013JD020475.
- [58] V. G. Ambrosia *et al.*, “An integration of remote sensing, GIS, and information distribution for wildfire detection and management,” *Photogramm. Eng. Remote Sens.*, vol. 64, no. 10, pp. 977–985, Oct. 1998.
- [59] J. T. Morissette, L. Giglio, I. Csizsar, and C. O. Justice, “Validation of the modis active fire product over Southern Africa with ASTER data,” *Int. J. Remote Sens.*, vol. 26, no. 19, pp. 4239–4264, Oct. 10, 2005, doi: 10.1080/01431160500113526.
- [60] L. Giglio *et al.*, “Active fire detection and characterization with the Advanced Spaceborne Thermal Emission and Reflection radiometer (ASTER),” *Remote Sens. Environ.*, vol. 112, no. 6, pp. 3055–3063, Jun. 16, 2008, doi: 10.1016/j.rse.2008.03.003.
- [61] P. H. Freeborn, M. J. Wooster, D. P. Roy, and M. A. Cochrane, “Quantification of MODIS fire radiative power (FRP) measurement uncertainty for use in satellite-based active fire characterization and biomass burning estimation,” *Geophys. Res. Lett.*, vol. 41, no. 6, pp. 1988–1994, 2014, doi: 10.1002/2013GL059086.
- [62] “Joint Polar Satellite System (JPSS) VIIRS Geolocation Algorithm Theoretical Basis Document (ATBD),” Joint Polar Satellite Syst. (JPSS), Lanham, MD, USA, 474-00053, Jul. 2011, Jul. 31, 2011. [Online]. Available: <http://npp.gsfc.nasa.gov/documents.html>
- [63] C. D. Elvidge, M. Zhizhin, F.-C. Hsu, and K. E. Baugh, “VIIRS nightfire: Satellite pyrometry at night,” *Remote Sens.*, vol. 5, no. 9, pp. 4423–4449, Sep. 2013, doi: 10.3390/rs5094423.
- [64] “Joint Polar Satellite System (JPSS) VIIRS Active Fires: Fire Mask Algorithm Theoretical Basis Document (ATDB),” Joint Polar Satellite Syst. (JPSS), Lanham, MD, USA, Apr. 2011, 474-00030, Apr. 22, 2011. [Online]. Available: <http://npp.gsfc.nasa.gov/documents.html>
- [65] P. J. Huber, “1972 Wald lecture—Robust statistics—Review,” *Ann. Math. Statist.*, vol. 43, no. 4, p. 1041, 1972, doi: 10.1214/aoms/1177692459.
- [66] C. Seielstad, J. Riddering, S. Brown, L. Queen, and W. Hao, “Testing the sensitivity of a MODIS-like daytime active fire detection model in alaska using NOAA/AVHRR infrared data,” *Photogramm. Eng. Remote Sens.*, vol. 68, no. 8, pp. 831–838, 2002.
- [67] D. A. Peterson *et al.*, “The 2013 rim fire: Implications for predicting extreme fire spread, pyroconvection, and smoke emissions,” *Bull. Amer. Meteorol. Soc.*, vol. 96, no. 2, pp. 229–247, Feb. 2015, doi: 10.1175/BAMS-D-14-00060.1.
- [68] C. L. Heald *et al.*, “Biomass burning emission inventory with daily resolution: Application to aircraft observations of asian outflow,” *J. Geophys. Res., Atmos.*, vol. 108, no. D21, p. 8811, 2003, doi: 10.1029/2002JD003082.
- [69] K. Muirhead and A. Cracknell, “Identification of gas flares in the north-sea using satellite data,” *Int. J. Remote Sens.*, vol. 5, no. 1, pp. 199–212, 1984.
- [70] O. C. D. Anejonu, G. A. Blackburn, and J. D. Whyatt, “Detecting gas flares and estimating flaring volumes at individual flow stations using modis data,” *Remote Sens. Environ.*, vol. 158, pp. 81–94, Mar. 2015, doi: 10.1016/j.rse.2014.11.018.
- [71] O. S. Ismail and G. E. Umukoro, “Global impact of gas flaring,” *Energy Power Eng.*, vol. 4, no. 4, pp. 290–302, Nov. 2012, doi: 10.4236/epe.2012.44039.
- [72] newsru.com, “Khanty-Mansi Autonomous District Extracted 10 Billion Tons of Oil,” 2012. [Online]. Available: <http://www.newsru.com/finance/22feb2012/ugra.html>
- [73] O. J. A. Bayode, E. A. Adewunmi, and S. Odunwole, “Environmental implications of oil exploration and exploitation in the coastal region of ondo state, nigeria: A regional planning appraisal,” *J. Geography Regional Plan.*, vol. 4, no. 3, pp. 110–121, Mar. 2011.
- [74] “Nigeria’s First National Communication Under the United Nations Framework Convention on Climate Change,” Ministry Environ. Federal Republic Nigeria, Abuja, Nigeria, 2003. [Online]. Available: <http://unfccc.int/resource/docs/natc/nigcn1.pdf>
- [75] “Estimated flared volumes from satellite data, 2007–2011,” World Bank, Washington, DC, USA, 2014. [Online]. Available: <http://go.worldbank.org/D03ET1BVDO>
- [76] D. Peterson, J. Wang, C. Ichoku, and L. A. Remer, “Effects of lightning and other meteorological factors on fire activity in the north american boreal forest: Implications for fire weather forecasting,” *Atmos. Chemistry Phys.*, vol. 10, no. 14, pp. 6873–6888, 2010, doi: 10.5194/acp-10-6873-2010.



Thomas N. Polivka received the B.S. degree in meteorology from Northern Illinois University, DeKalb, IL, USA, and the M.S. degree in atmospheric science from the University of Nebraska—Lincoln, Lincoln, NE, USA.

He is currently with the Department of Earth and Atmospheric Sciences, University of Nebraska—Lincoln. His research interests include the use of satellite-based measurements for fire detection and characterization.



Jun Wang received the B.S. degree in meteorology from Nanjing Institute of Meteorology, Nanjing, China; the M.S. degree in atmospheric dynamics from the Institute of Atmospheric Physics, Chinese Academy of Sciences, Beijing, China; and the Ph.D. degree in atmospheric science from the University of Alabama, Huntsville, AL, USA.

In 2005–2007, he was a Postdoctoral Researcher with Harvard University, Cambridge, MA, USA, before joining the University of Nebraska—Lincoln, Lincoln, NE, USA, as a faculty member. His research interests include satellite remote sensing of aerosols and fires, chemistry transport modeling, data assimilation, inverse optimization, and integration of these elements to study air quality and aerosol–cloud interaction.



Luke T. Ellison received the B.A. degree in engineering science and Physics from Bethel University, St. Paul, MN, USA, and the Bachelor’s degree in aerospace engineering and mechanics from the University of Minnesota Twin Cities, Minneapolis, MN, USA, both in 2007.

After working at Cessna Aircraft Company, Wichita, KS, USA, as a Sustaining Engineer for the Citation Mustang entry-level business jet, he accepted a research position in 2009 in the Climate and Radiation Laboratory, NASA Goddard Space Flight Center, Greenbelt, MD, USA. His research at Goddard centers around the remote sensing of wildfires, and has included endeavors such as validation of the two Moderate Resolution Imaging Spectroradiometer (MODIS) instruments, development of a new biomass burning emissions inventory, research on the interactions and feedback between biomass burning and the hydrological cycle in Northern Sub-Saharan Africa, advocating for an increase and improvement of the available airborne and spaceborne fire-sensing platforms, and development and maintenance of the FEER project website (<http://feer.gsfc.nasa.gov/>).



Edward J. Hyer received the Ph.D. degree in geography from The University of Maryland, College Park, MD, USA.

He is currently a Physical Scientist with the Marine Meteorology Division, Naval Research Laboratory, Monterey, CA, USA. His research interests include remote sensing of fires and aerosols, modeling of biomass burning emissions, and data assimilation for air quality modeling.



Charles M. Ichoku received the B.Sc. and M.Sc. degrees in surveying sciences from the University of Nigeria, Nsukka, Nigeria, in 1982 and 1987, respectively, and the the DESS (Diplôme d'Etudes Supérieures Spécialisées) degree in remote sensing and the Ph.D. degree in earth sciences from Pierre et Marie Curie Sorbonnes Universités, Paris, France, in 1989 and 1993, respectively.

From 1993 to 1997, he was a Research Fellow/Visiting Scientist with the Jacob Blaustein Institute for Desert Research, Ben-Gurion University of the Negev, Sede Boqer Campus, Sede Boqer, Israel, and from 1997 to 1998, with the Max-Planck Institute for Chemistry, Mainz, Germany. His research interests activities include the development of remote sensing applications in various branches of Earth sciences, including geology, hydrology, and atmospheric studies. In November 1998, he joined the NASA Goddard Space Flight Center, Greenbelt, MD, USA, as a Research Scientist. His research interests have been in remote sensing of aerosols and fires, their global distribution, and their impacts on the human population, the environment, and climate. He has been actively involved in various interdisciplinary research activities and project/program leadership roles, and is currently leading a NASA interdisciplinary research project investigating the anthropogenic influences on the water cycle dynamics in the northern sub-Saharan African region.

Dr. Ichoku is a member of the American Geophysical Union AGU.